

PULSE NMR IN SOLIDS:  
CHEMICAL SHIFT, LEAD FLUORIDE AND THORIUM HYDRIDE

Thesis by  
Kei-Fung Lau

In Partial Fulfillment of the Requirements  
for the Degree of  
Doctor of Philosophy

California Institute of Technology  
Pasadena, California

1976

(Submitted May 24, 1976)

*To my parents*

ACKNOWLEDGEMENTS

I would like to express my deepest gratitude to my advisor Professor Robert W. Vaughan, for without his suggestions and guidances this thesis would not have been possible. Professor Vaughan not only arranged for my graduate assistantships throughout my years in Caltech but also coached me in all aspects of this thesis research. His special enthusiasm in science and his ability to perceive insights to specific problems much faster than anyone else I have known have been a constant amazement and inspiration to me.

I am fortunate also to have shared an office for nearly four years with my friend and colleague, Dr. Loren B. Schreiber. We learned NMR, discussed about our research programs and talk about physics, chemistry, life, philosophy and many other things together. I have always admired his hard working attitude, his logical thinking and his keen sense of humor.

My special appreciation goes to my wife, Lesly, whose love and patience give me much happiness and encouragement.

Mrs. Sharon ViGario, my wife Lesly and my brother David Kei-Sau Lau all contributed to the preparation of this thesis. For this I give them thanks.

ABSTRACT

Part one of this thesis consists of two sections. In the first section the fluorine chemical shift of a single crystal  $\text{CaF}_2$  has been measured as a function of external pressure up to 4 kilobar at room temperature using multiple pulse NMR techniques. The pressure dependence of the shift is found to be  $-1.7 \pm 1$  ppm/kbar, while a theoretical calculation using an overlap model predicts a shift of  $-0.46$  ppm/kbar. In the second section a separation of the chemical shift tensor into physically meaningful "geometrical" and "chemical" contributions is presented and a comparison of the proposed model calculations with recently reported data on hydroxyl proton chemical shift tensors demonstrates, that for this system, the geometrical portion accounts for the qualitative features of the measured tensors.

Part two of the thesis consists of a study of fluoride ion motion in  $\beta\text{-PbF}_2$  doped with NaF by measurement of the  $^{19}\text{F}$  transverse relaxation time ( $T_2$ ), spin lattice relaxation time ( $T_1$ ) and the spin lattice relaxation time in the rotating frame ( $T_{1r}$ ). Measurements over the temperature range of  $-50^\circ\text{C}$  to  $160^\circ\text{C}$  lead to activation energies for  $T_1$ ,  $T_{1r}$  and  $T_2$  of  $0.205 \pm 0.01$ ,  $0.29 \pm 0.02$  and  $0.27 \pm 0.01$  eV/ion, and a  $T_{1r}$  minimum at  $56^\circ\text{C}$  yields a correlation time of  $0.74$   $\mu\text{sec}$ . Pressure dependence of  $T_1$  and  $T_2$  yields activation volumes of  $<0.2$   $\text{cm}^3/\text{g-mole}$  and  $1.76 \pm 0.05$   $\text{cm}^3/\text{g-mole}$  respectively. These data along with the measured magnetic field independence of  $T_1$  suggest that the measured  $T_1$ 's are not caused by  $^{19}\text{F}$  motion, but by thermally excited carriers.

Part three of the thesis consists of a study of two samples of  $\text{Th}_4\text{H}_{15}$ , prepared under different conditions but both having the proper ratio of H/Th (to within 1%). The structure of the  $\text{Th}_4\text{H}_{15}$  as suggested by X-ray measurements is confirmed through a moment analysis of the rigid lattice line shape.  $T_1$  and  $T_2$  measurements above 390 K furnish activation energies of  $16.3 \pm 1.2$  kcal/mole and  $18.0 \pm 3.0$  kcal/mole, respectively. Below 350 K,  $T_{1r}$  measurements furnish an activation energy of  $10.9 \pm 0.7$  kcal/mole, indicating most probably more than a single mechanism for proton motion. A time-temperature hysteresis effect of the proton motion was found in one of the two samples and is strongly indicative of a phase change.  $T_1$  at room temperature and below is dominated by relaxation due to conduction electrons with the product  $T_1T$  being  $180 \pm 10$  K-sec. Using multiple pulse techniques to greatly reduce homonuclear dipolar broadening, a temperature-dependent line shift was observed, and the chemical shift anisotropy is estimated to be less than 16 ppm.

TABLE OF CONTENTS

	<u>Page</u>
ACKNOWLEDGEMENTS	iii
ABSTRACT	iv
I. GENERAL INTRODUCTION	1
Figure	4
II. CHEMICAL SHIFT MEASUREMENT AND INTERPRETATION	5
Introduction	6
Pressure Dependence of $^{19}\text{F}$ Chemical Shift in $\text{CaF}_2$	10
Proton Chemical Shift Tensors	21
Conclusion	38
References	39
Tables	42
Figures	46
III. FLUORIDE ION MOTION IN DOPED $\beta\text{-PbF}_2$	51
Introduction	52
Experimental Details	52
Experimental Results	53
Discussion and Conclusions	57
References	62
Tables	63
Figures	65
IV. NMR Study of $\text{Th}_4\text{H}_{15}$	70
Introduction	71

TABLE OF CONTENTS (Continued)

	<u>Page</u>
Experimental Details	72
Results and Discussion	74
A. Rigid Lattice Lineshape	74
B. Relaxation Times and Motional Properties	77
C. Multiple pulse Measurements and Knight Shift	82
References	86
Figures	88

CHAPTER 1  
GENERAL INTRODUCTION

It was first suggested by Pauli (1924) and was later confirmed that many atomic nuclei in their ground states possess intrinsic angular momentum (spin) and magnetic moment. In Nuclear Magnetic Resonance spectroscopy one observes macroscopic effects of the magnetic moments associated with the nuclear spins. Since nuclear spins are microscopic in nature NMR provides a unique way to obtain microscopic informations on the physical and chemical properties of the material containing the spins.

Important progress has been made on the theory of NMR since the first detection of nuclear signal in 1946. Its application has been wide-spread: ranging from the field of nuclear physics, solid state physics, pure and applied chemistry, metallurgy to the field of biology, geophysics etc. Yet, even after 30 years of extensive research, new techniques and new applications are continuously being discovered.

This thesis research concentrates on the problems related to the use of NMR spectroscopy in the investigation of solids. The laboratory at Caltech in which most of the experiments were done is particularly well equipped for this purpose. The pulse spectrometer, as shown in Figure 1, operates at 56.4 MHz and is capable of performing various pulse cycles including the 8 pulse cycle which eliminates the dipole-dipole interaction of the nuclear spins in solids and allows measurements of smaller details such as chemical shift tensor. During the course of the present research different NMR probes were built to improve the 8 pulse performance and to allow measurements at various temperatures or pressures. The capabilities and flexibilities of the

spectrometer has a large influence on the type of studies pursued.

The nuclei studied in this thesis are mainly proton and fluorine ( $^{19}\text{F}$ ), either one of which has spin  $\frac{1}{2}$  and neither possesses an electrical quadrupole moment. In spite of these restrictions the three parts of the thesis contain a wide spectrum of topics in the field of NMR spectroscopy. The first part contains a study of pressure dependent chemical shift in ionic solids and a theoretical interpretation of the proton chemical shift tensors in diamagnetic solids. The second part contains a study of ionic motion in a superionic conductor,  $\beta\text{-PbF}_2$  doped with NaF. In the last part a metal hydride,  $\text{Th}_4\text{H}_{15}$ , is studied. The materials studied range from diamagnetic solids to metals; the phenomena observed include resonance line shift and spin relaxation effects; and the techniques used consist of conventional pulse techniques and the newly developed pulse cycles. In short, this thesis represents an attempt to further the use of NMR in the study of solids and in each case definite progress has been made.

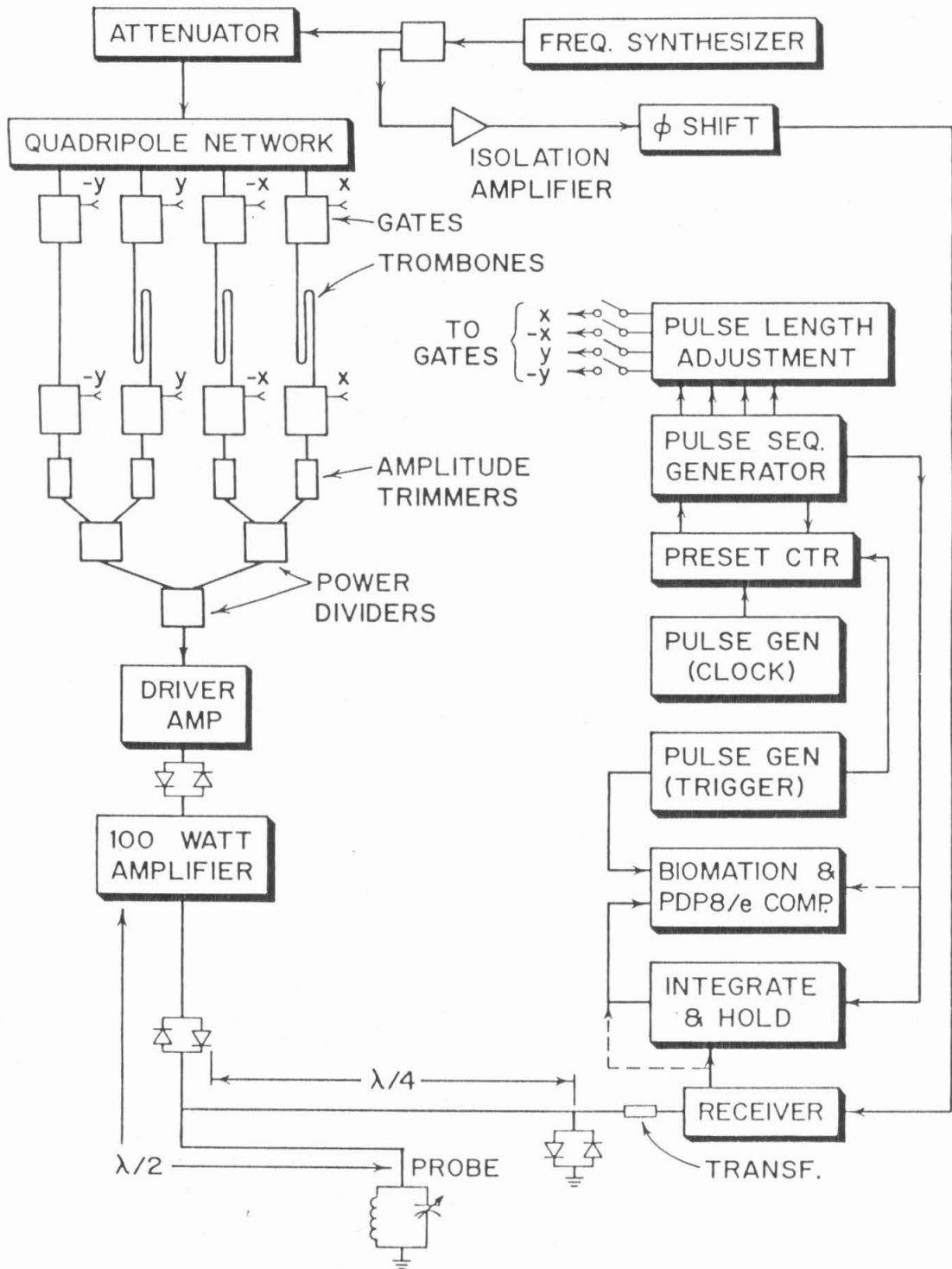


Fig. 1. Schematic diagram of the pulse spectrometer.

CHAPTER 2  
CHEMICAL SHIFT MEASUREMENT AND INTERPRETATION

## INTRODUCTION

A nucleus in bulk matter is surrounded by electrons and other nuclei, and the nuclear spin can serve as a probe to obtain information on this environment through its interaction with the surrounding electrons and nuclei. When materials containing nuclear spins are placed in a magnetic field the Hamiltonian for the spins can be written as

$$H_{\text{total}} = H_{\text{nz}} + H_{\text{en}} + H_{\text{d}} + H_{\text{q}} \quad (1)$$

where  $H_{\text{nz}}$  = interaction with the applied field; nuclear Zeeman interaction

$H_{\text{en}}$  = interaction with the electrons

$H_{\text{d}}$  = dipolar interaction among nuclear spins

$H_{\text{q}}$  = quadrupolar interaction with the electric field gradient

The term  $H_{\text{en}}$  consists of  $H_{\text{c}}$  : interaction with the orbital motion of electronic charges ( chemical shift );  $H_{\text{k}}$  : interaction with the magnetic moment of electron spins ( Knight shift ); and  $H_{\text{ss}}$  : nuclear spin-spin coupling<sup>(1)</sup>. The last term is included here because it is a second order effect of electron nuclear interaction.

The parameter  $\vec{\sigma}$  characterizing the chemical shift is defined by the equation

$$H_{\text{c}} = \vec{\mu} \cdot \vec{\sigma} \cdot \vec{H} \quad (2)$$

where  $\vec{\mu}$  is the magnetic moment of the nucleus;  $\vec{H}$  is the applied magnetic field; and  $\vec{\sigma}$  is the parameter referred to as chemical shift tensor. If all interactions in Equation 1 except  $H_{nz}$  and  $H_c$  are absent, the magnetic field seen by a nucleus is

$$H_{\text{eff.}} = H (1 - \sigma_{zz}) \quad (3)$$

where the external field  $\vec{H}$  is taken to be in the z direction. The experimental measurement allows only the determination of the relative shift  $\vec{\delta}$  with respect to a reference standard. Typically, the range of  $\delta_{zz}$  for proton is at the order of 10 ppm, while that of heavier nuclei such as  $^{19}\text{F}$  and  $^{13}\text{C}$  the  $\delta_{zz}$  is at the order of 100 ppm or more<sup>(2)</sup>.

The measurement of chemical shift is one of the main task of NMR spectroscopy since chemical shift is found to be very useful in correlating and understanding electronic structures of numerous materials. The electronic structure around a nucleus is dependent on the chemical environment of the nucleus; the chemical shift which measures the electron-nuclear interaction reflects the chemical state of the material. Small variations in the electronic states due to variation of external parameters such as temperature, pressure, concentration ... etc. can be studied by chemical shift measurements.

Traditionally most chemical shift measurements are done in liquids where the  $H_d$  in Equation 1 is averaged out due to the rapid random motion of the nuclei. In most solids under normal laboratory magnetic field  $H_d$  is much larger than  $H_c$  and as a result the NMR line is broadened so much that the measurement of chemical shift is impossible. With the recently developed multiple pulse techniques 99.5% or more of

the dipolar interaction can be eliminated and the chemical shift information is recovered. In addition, if a single crystal is used not only the isotropic part but all six components of the symmetric part of the tensor can be measured<sup>(3 - 7)</sup>.

The original theory of chemical shift was proposed by Ramsey<sup>(8)</sup>. In his derivation the absolute shift  $\vec{\sigma}$  is separated into diamagnetic and paramagnetic terms. Direct application of the theory is difficult and becomes even more so for large molecules and extended solids. To reduce this problem Saika and Slichter<sup>(9)</sup> proposed that the chemical shift is essentially due to electrons near the shielded nucleus and good estimate of the shift can be obtained by considering only the local paramagnetic and diamagnetic terms, both of which are from contributions of electrons in the orbitals centered on the shielded nucleus. The contributions from electrons on other centers can then be considered as bulk susceptibility effect. This localized theory has been quite useful in estimating the shifts in large molecules containing nuclei such as  $^{19}\text{F}$  and  $^{13}\text{C}$ <sup>(10)</sup>. However, for proton chemical shifts the local contribution around the proton seems inadequate to account for the experimental results. It is recognized that since the total shielding of the proton is small the neighbor effect may become one of the dominating factors<sup>(2)</sup>.

The purpose of this part of the research is to extend the experimental and theoretical study of chemical shift tensors in solids. In the first section the technique which eliminates nuclear dipole-dipole interaction and allows measurement of small chemical shifts is applied to the measurement of the shift of  $^{19}\text{F}$  in  $\text{CaF}_2$  as a function of

hydrostatic pressures in the 4 kbar range. A calculation of the pressure dependent shift using Ramsey's formulation is also presented and compared with the measurement to provide a test of this formalism. In the second section the theory of chemical shift as applied to proton is re-examined. Instead of trying more and more complicated calculations of the total shift a new interpretation is proposed which follows the same principle that motivates the localized theory mentioned above. Namely, the chemical shift tensor is to be explained and understood by seeking out the dominant contributions which can be estimated rather simply. In this way some of the confusions in the existing theories of proton chemical shift tensors are clarified.

PRESSURE DEPENDENCE OF  $^{19}\text{F}$  CHEMICAL SHIFT IN  $\text{CaF}_2$

BACKGROUND

Chemical shifts have been measured in a number of ionic solids<sup>(11-13)</sup>. In most cases, the shifts have been interpreted with an overlap model originally proposed by Kondo and Yamashita<sup>(14)</sup>. A useful and stringent test of this interpretation is to compare the calculated and experimental pressure dependence of the chemical shift in such solids. During pressure experiments only the interatomic distance is varied, and the overlap model makes a clear prediction of the pressure dependence of the chemical shift which can be compared directly with experiment. Measurements of this type have been performed on heavy ions  $^{87}\text{Rb}$ ,  $^{137}\text{Cs}$ ,  $^{127}\text{I}$ ,  $^{81}\text{Br}$ , and  $^{35}\text{Cl}$  in  $\text{RbCl}$ ,  $\text{RbBr}$ ,  $\text{RbI}$ ,  $\text{CsBr}$ , and  $\text{CsI}$ <sup>(13)</sup>. In the present work the pressure dependence of the chemical shift of  $^{19}\text{F}$  in  $\text{CaF}_2$  is reported. The relatively simpler electronic wavefunctions of the lighter fluoride ion allow testing of the various aspects of the overlap model with more precision and less ambiguity since better Hartree-Fock wavefunctions are available for the fluoride ion than the heavier halides treated earlier<sup>(13)</sup>.

### EXPERIMENTAL ARRANGEMENTS

In this measurement an eight-pulse cycle<sup>(4)</sup> is used to eliminate the  $^{19}\text{F}$ - $^{19}\text{F}$  dipolar interaction and allow measurement of the  $^{19}\text{F}$  chemical shift. The probe for the spectrometer was specially constructed with a coil of 5 mm in diameter and located inside a beryllium-copper high pressure cell. The coil has about 12 turns and is made of flattened copper wire to improve the rf homogeneity. The pressure cell was patterned after the type used by Benedek<sup>(15)</sup> with a design pressure range of 8 kbar, but the system was used only up to 4 kbar. The pressure was transmitted by hydraulic oil and was measured by a Heise-Burbon tube gauge to 0.1% accuracy. A single crystal of  $\text{CaF}_2$  was cut into a spherical shape and was attached to a nylon rod which could be screwed in place inside the high pressure cell. The purpose of this was so that the orientation of the crystal could be adjusted while the probe was in the magnetic field and that orientation could remain fixed during the pressure experiment as the pressure fluid is moving in and out of the cell.

The symmetry of the fluorine site in  $\text{CaF}_2$  is cubic, and the chemical shift tensor is therefore isotropic. Thus, the chemical shift is independent of the orientation of the crystal; however, the dipolar interaction is dependent on the orientation of the crystal, and it was desirable to make measurements with the magnetic field oriented parallel to the [111] crystallographic axis where the line narrowing is the most efficient. An internal calibration scheme was devised since the application of pressure causes some detuning of the probe which can affect the measurements made with the eight-pulse cycle<sup>(5)</sup>. To allow determination of the chemical shift independent of such effects, a

differential measurement was made by including a small amount of liquid  $C_6F_6$  sealed inside a spherical glass bead, inside the coil near the  $CaF_2$  sample. As pressure was applied, the resonance peaks of both the  $CaF_2$  and  $C_6F_6$  were measured simultaneously. Since a small air bubble was formed inside the glass bead before and after the pressure experiment, some leeway was provided for the glass to contract and still maintain the  $C_6F_6$  near atmospheric pressure at all times.

### THE MEASURED SHIFT

The measured shift is shown in Figure 1. The shift induced by pressure is  $-1.7 \pm 1$  ppm/kbar. There was scattering (2-3 ppm) of the measured difference between the reference peak and the  $CaF_2$  peak since the separation was large, 61 ppm or more, and the line width of the  $CaF_2$  was  $\sim 5$  ppm. The 5 ppm line width was present because one had to go off resonance enough to allow the two peaks to simultaneously be viewed on the same side of resonance and the  $H_1$  inhomogeneity off-resonance cross term in the Hamiltonian<sup>(5)</sup> became large. The  $CaF_2$  peak was, thus, too far off resonance to have the best resolution, and the error limit has been set at  $\pm 1$  ppm/kbar.

### CALCULATION OF THE CHEMICAL SHIFT

The small differences in the resonance frequency that are observed when the chemical environment of the  $^{19}F$  is altered can be discussed in terms of electronic wavefunctions and charge distributions near the  $^{19}F$  nuclei. The theoretical basis for such an interpretation was initially formulated by Ramsey<sup>(8)</sup> and is applied here to calculate the

pressure dependence of the  $^{19}\text{F}$  shift in  $\text{CaF}_2$ . Ramsey's formulation separated the shielding tensor into two components: a diamagnetic term which is calculated from ground state wavefunctions and a paramagnetic term which involves a summation over all excited states. As knowledge of the excited state wavefunctions is normally not available, exact calculation of the paramagnetic term is not possible. Ramsey suggested that the average energy approximation of Van Vleck and Frank<sup>(16)</sup> could be applied to remove the summation over excited states and thus furnish a means of obtaining an approximation to the paramagnetic term from knowledge of only ground state wavefunctions. Although widely used, this approximation has received criticism<sup>(17)</sup> and can be justified primarily by its success in accounting for observed shifts<sup>(18)</sup>. Alternate approaches<sup>(18-22)</sup>, including the use of variational techniques, have been developed to attempt to circumvent this difficulty inherent in the second-order perturbation formulation and have succeeded in giving good agreement with experiment for small molecules. The average energy approximation approach was used in the overlap model of chemical shift in ionic solids by Kondo and Yamashita<sup>(14)</sup> and has given correct qualitative predictions where it has been applied to calculations of the pressure dependence of the chemical shifts in the heavier halides<sup>(23,24)</sup>, and it is used here to attempt to account for the observed pressure dependence in  $\text{CaF}_2$ .

In this overlap model the paramagnetic term is seen to arise mainly from the overlap of the ionic wavefunctions among nearest-neighbor ions, and the pressure data are particularly useful because one can test directly the dependence of the shift on the amount of overlap between ionic wavefunctions.

The following formulations and notations are similar to that by Ikenberry and Das<sup>(23)</sup> in their calculation of chemical shift in alkali halides and also to that by Vaughan, et al. in their calculation for MgF<sub>2</sub><sup>(12)</sup>.

From Ramsey's equation, using the average energy approximation and the closure relationship<sup>(23)</sup>, one obtains the following relationships for the chemical shift:

$$\begin{aligned} \sigma &= \sigma^d + \sigma^p \\ &= \left( \frac{e^2}{2mc^2} \right) \langle \Psi_0 | \sum_k [\vec{I} \cdot (\vec{r}_k - \vec{R}_{k1}) \vec{r}_k - (\vec{r}_k - \vec{R}_{k1}) \cdot \vec{r}_k] / r_k^3 | \Psi_0 \rangle \\ &\quad - \left( \frac{e^2}{\Delta E m^2 c^2} \right) \langle \Psi_0 | \sum_{k,k'} (\vec{I}_{k0} \vec{I}_{k1}) / r_k^3 | \Psi_0 \rangle \end{aligned} \quad (4)$$

where the ground state wavefunction

$$\begin{aligned} \Psi_0 &= \frac{1}{\sqrt{2n!}} | \Psi_{1 \uparrow(1)} \Psi_{1 \downarrow(2)} \dots \Psi_{n \uparrow(2n-1)} \Psi_{n \downarrow(2n)} | \\ \Psi_i &= \phi_i - \frac{1}{2} \sum_j S_{ij} \phi_j + \frac{3}{8} \sum_{jk} S_{ik} S_{kj} \phi_j - \dots \\ S_{ij} &= \langle \phi_i | \phi_j \rangle - \delta_{ij} \end{aligned} \quad (5)$$

↑ or ↓ denotes the spin part of the one electron wavefunction, and the spatial part is

$$\Psi_i = \phi_i - \frac{1}{2} \sum_j S_{ij} \phi_j + \frac{3}{8} \sum_{jk} S_{ik} S_{kj} \phi_j - \dots$$

in which  $S_{ij} = \langle \phi_i | \phi_j \rangle - \delta_{ij}$  is the overlap between ionic wavefunctions  $\phi_i$  and  $\phi_j$  of free ions.  $\Psi_i$  defined in this manner is the

Löwdin orthogonalized atomic orbital<sup>(25)</sup>.  $\vec{r}_k$  is the position of electron  $k$  from the nucleus of interest.  $\vec{R}_{k1}$  is a vector from the nucleus of interest to the location of the vector potential gauge center for the electron  $k$ .  $\vec{I}$  is the unit dyadic;  $\vec{l}_{k1}$  is the angular momentum operator,  $-\hbar(\vec{r} - \vec{R}_{k1}) \times \vec{\nabla}_k$ . From the location of the gauge for electron  $k$ ,  $\Delta E$  is the "average excitation energy."

Note that Equation 1 is written in a form such that one can arbitrarily choose the gauge for the vector potential of each electron; however, this is clearly not possible for an electron in an antisymmetrized wavefunction. It is possible, however, to use an appropriate gauge choice for the noninteracting electrons, i.e., the core electrons on the ions which do not overlap to any extent with neighboring ions, to evaluate their contribution to Equation 1. That is, for electrons forming filled shells and so tightly bound that their mean potential is spherical, the sum of  $\sigma^d$  and  $\sigma^p$  will be small and in the form of a point dipolar field at a position outside of the ion in question<sup>(8)</sup>, as can be most easily seen with a gauge centered at the nuclear site of the electronic wavefunctions in question. For the cubic structure of interest here, such terms will contribute only in the long-range bulk susceptibility term.

Thus, for the calculation done here the only electrons considered for Equation 1 are the outer  $s$  and  $p$  electrons on both the fluorine and calcium as well as the core electrons on the fluorine site for which the calculation is being done. Thus, Equation 1 is converted to a summation of contributions from each of these remaining orbitals in Equations 3 and 4 and with a gauge choice centered at the fluorine site where the

magnetic shielding is being calculated.

$$\sigma^d = \frac{2}{3} \alpha^2 \sum_j \langle \psi_j | \frac{1}{r_0} | \psi_j \rangle \quad (6)$$

$$\sigma_{xx}^p = -\frac{4\alpha^2}{\Delta} \left[ \sum_j \langle \psi_j | \frac{1}{r_0} \frac{x_0^2}{3} | \psi_j \rangle - \sum_{j \neq j'} \langle \psi_j | \frac{1}{r_0} \frac{x_0}{3} | \psi_{j'} \rangle \right. \\ \left. \times \langle \psi_{j'} | \frac{1}{r_0} x_0 | \psi_j \rangle \right] \quad (7)$$

where  $\alpha$  = the fine structure constant

and  $\Delta$  = the average energy in Rydberg

$r$  = units of Bohr radius (the spin multiplicity of 2 is included).

If one evaluates Equations 3 and 4 with this particular choice of gauge, one finds that for electron density located far from the nucleus of interest both  $\sigma^d$  and  $\sigma^p$  receive large contributions of opposite sign. That the total contribution to the chemical shift,  $\sigma$ , from electrons located far from the point of interest should be small has long been recognized<sup>(26)</sup>, and the large and canceling contributions to  $\sigma^d$  and  $\sigma^p$  are artifacts of the gauge choice. For these reasons previous authors<sup>(26)</sup> have concentrated on calculating the local contributions to  $\sigma^d$  and  $\sigma^p$  and have corrected, if at all, for the longer-range effects with a bulk susceptibility correction determined experimentally.

Considering first the paramagnetic term,  $\sigma^p$ , the local contribution includes all terms such as  $\langle \phi_0 | 0p. | \phi_j \rangle$ , and the ions in consideration include the fluorine at the center together with four calciums and six fluoride ions as shown in Figure 2. Under these conditions, Equation 4

simplifies to:

$$\begin{aligned}
 \sigma_{xx}^p = & -\frac{16\alpha^2}{\Delta} \left\{ \langle \phi_{oy} \mid \frac{1}{r_o} \mid \phi_{oy} \rangle [ |S_{oj}^{\sigma s}|^2 + |S_{oj}^{\sigma\sigma}|^2 + 2 |S_{oj}^{\pi\pi}|^2 ] \right. \\
 & - 2S_{oj}^{\sigma s} \langle \phi_{o\sigma} \mid \frac{1}{r_o} \mid \phi_{js} \rangle - 2S_{oj}^{\sigma\sigma} \langle \phi_{o\sigma} \mid \frac{1}{r_o} \mid \phi_{j\sigma} \rangle \\
 & \left. - 4S_{oj}^{\pi\pi} \langle \phi_{o\pi} \mid \frac{1}{r_o} \mid \phi_{j\pi} \rangle \right\} \\
 & - \frac{32\alpha^2}{3\Delta} \left\{ \langle \phi_{oy} \mid \frac{1}{r_o} \mid \phi_{oy} \rangle [ |S_{oj}^{\sigma s}|^2 + |S_{oj}^{\sigma\sigma}|^2 + 2 |S_{oj}^{\pi\pi}|^2 ] \right. \\
 & - 2S_{oj}^{\sigma s} \langle \phi_{o\sigma} \mid \frac{1}{r_o} \mid \phi_{js} \rangle - 2S_{oj}^{\sigma\sigma} \langle \phi_{o\sigma} \mid \frac{1}{r_o} \mid \phi_{j\sigma} \rangle \\
 & \left. - 4S_{oj}^{\pi\pi} \langle \phi_{o\pi} \mid \frac{1}{r_o} \mid \phi_{j\pi} \rangle \right\} \quad (8)
 \end{aligned}$$

where the first three lines involve the orbitals of the center fluorine with subscript, o, and the neighbor fluorine with subscript, j. The last three lines involve the center fluorine and the calcium orbitals with subscript, j. The overlap between non-next neighbors is neglected, and since the S's are small, only terms up to the order  $S^2$  are retained. All integrals of the type  $\langle \phi_i \mid 0p. \mid \phi_j \rangle$  are neglected if neither of the  $\phi_i$ ,  $\phi_j$ , nor  $0p.$  are located at the center fluorine. Previous authors<sup>(23)</sup> have used a somewhat different approximation. They have not excluded all nonlocal

integrals of the type  $\langle \phi_i | 0_p | \phi_j \rangle$  but have included terms of the type  $\langle \phi_{jy} | 1_{x0} | \phi_{jz} \rangle$  while neglecting terms of the form  $\langle \phi_{js} | 1_{x0} | \phi_{jy} \rangle$ . This is inconsistent since one can show that the ignored terms are larger than those included. That is,

$$\langle \phi_{js} | 1_{x0} | \phi_{jy} \rangle = \langle \phi_{js} | 1_{xj} | \phi_{jy} \rangle + \langle \phi_{js} | Y \frac{\partial}{\partial z} - Z \frac{\partial}{\partial y} | \phi_{jy} \rangle \quad (9)$$

and the second term is of order unity and clearly can be neglected only if one wishes to calculate the local contributions to  $\sigma^p$ . For comparison, the paramagnetic term calculated in this previous approximation is:

$$\begin{aligned} \sigma_{xx}^p = & - \frac{16\alpha^2}{\Delta} \left\{ \langle \phi_{oy} | \frac{1}{r_0} | \phi_{oy} \rangle [ |S_{oj}^{\sigma s}|^2 + |S_{oj}^{\sigma\sigma}|^2 + |S_{oj}^{\pi\pi}|^2 - 2S_{oj}^{\sigma\sigma} S_{oj}^{\pi\pi} ] \right. \\ & + 2(S_{oj}^{\sigma\sigma} - S_{oj}^{\pi\pi}) [ \langle \phi_{o\pi} | \frac{1}{r_0} | \phi_{j\pi} \rangle - \langle \phi_{o\sigma} | \frac{1}{r_0} | \phi_{j\sigma} \rangle ] \\ & \left. - 2S_{oj}^{\sigma s} \langle \phi_{js} | \frac{1}{r_0} | \phi_{o\sigma} \rangle \right\} \\ & - \frac{32\alpha^2}{3\Delta} \left\{ \langle \phi_{oy} | \frac{1}{r_0} | \phi_{oy} \rangle [ |S_{oj}^{\sigma s}|^2 + |S_{oj}^{\sigma\sigma}|^2 + |S_{oj}^{\pi\pi}|^2 - 2S_{oj}^{\sigma\sigma} S_{oj}^{\pi\pi} ] \right. \\ & + 2(S_{oj}^{\sigma\sigma} - S_{oj}^{\pi\pi}) [ \langle \phi_{o\pi} | \frac{1}{r_0} | \phi_{j\pi} \rangle - \langle \phi_{o\sigma} | \frac{1}{r_0} | \phi_{j\sigma} \rangle ] \\ & \left. - 2S_{oj}^{\sigma s} \langle \phi_{js} | \frac{1}{r_0} | \phi_{o\sigma} \rangle \right\} \quad (10) \end{aligned}$$

For the diamagnetic term, one obtains:

$$\sigma^d = \sigma_F^d + \sigma_{\text{overlap}}^d \quad (11)$$

$\sigma_F^d$  is the contribution due to the fluorine ion at the center.

$$\begin{aligned} \sigma_{\text{overlap}}^d = & 4\alpha^2 \{ \langle \phi_{oy} | \frac{1}{r_0} | \phi_{oy} \rangle ( |S_{oj}^{\sigma s}|^2 + |S_{oj}^{\sigma\sigma}|^2 + 2 |S_{oj}^{\pi\pi}|^2 ) \\ & + \langle \phi_{os} | \frac{1}{r_0} | \phi_{os} \rangle ( |S_{oj}^{ss}|^2 + |S_{oj}^{s\sigma}|^2 ) - 2 [ S_{oj}^{ss} \langle \phi_{os} | \frac{1}{r_0} | \phi_{js} \rangle \\ & + S_{oj}^{s\sigma} \langle \phi_{os} | \frac{1}{r_0} | \phi_{j\sigma} \rangle + S_{oj}^{\sigma s} \langle \phi_{o\sigma} | \frac{1}{r_0} | \phi_{js} \rangle + 2 S_{oj}^{\pi\pi} \langle \phi_{o\pi} | \frac{1}{r_0} | \phi_{j\pi} \rangle \\ & + S_{oj}^{\sigma\sigma} \langle \phi_{o\sigma} | \frac{1}{r_0} | \phi_{j\sigma} \rangle ] \} \\ & + \frac{8}{3}\alpha^2 \{ \langle \phi_{oy} | \frac{1}{r_0} | \phi_{oy} \rangle ( |S_{oj}^{\sigma s}|^2 + |S_{oj}^{\sigma\sigma}|^2 + 2 |S_{oj}^{\pi\pi}|^2 ) \\ & + \langle \phi_{os} | \frac{1}{r_0} | \phi_{os} \rangle ( |S_{oj}^{ss}|^2 + |S_{oj}^{s\sigma}|^2 ) - 2 [ S_{oj}^{ss} \langle \phi_{os} | \frac{1}{r_0} | \phi_{js} \rangle \\ & + S_{oj}^{s\sigma} \langle \phi_{os} | \frac{1}{r_0} | \phi_{j\sigma} \rangle + S_{oj}^{\sigma s} \langle \phi_{o\sigma} | \frac{1}{r_0} | \phi_{js} \rangle + 2 S_{oj}^{\pi\pi} \langle \phi_{o\pi} | \frac{1}{r_0} | \phi_{j\pi} \rangle \\ & + S_{oj}^{\sigma\sigma} \langle \phi_{o\sigma} | \frac{1}{r_0} | \phi_{j\sigma} \rangle ] \} \end{aligned} \quad (12)$$

The first four lines are for F-F overlap, and the last four lines for

the F-Ca overlap.

The evaluation of the above equations requires the value of overlap integrals at different pressures. The atomic spacings at different pressures are obtained from Bridgman's compressibility data<sup>(27)</sup>. The overlap integrals at those atomic spacings are calculated on a computer using Clementi's Hartree-Fock wavefunctions<sup>(28)</sup>. Part of the integrals pertinent to the pressure calculation are shown in Table 1. One can use the calculated absolute shift of  $\text{CCl}_3\text{F}$  (188.7 ppm)<sup>(29)</sup> together with measured differential shifts between  $\text{CaF}_2$  and  $\text{C}_6\text{F}_6$  (-61 ppm) and the reported shift of  $\text{C}_6\text{F}_6$  relative to  $\text{CCl}_3\text{F}$  (+164.9 ppm)<sup>(30)</sup> to assign an absolute shift of 292.6 ppm to  $\text{CaF}_2$ . The diamagnetic term as calculated from equations 11 and 12 is 482.25 ppm, and thus, by difference, the paramagnetic term as defined in Equation 7 is 189.65 ppm. This value for  $\sigma^{\text{P}}$  can be used to fit the average energy parameter,  $\Delta$ , in Equation 7, and one obtains a value of 0.47 Rydberg with Equation 8. Pressure dependence can be obtained by reevaluating Equations 7 and 8 for overlap integrals appropriate for the high pressure condition and assuming that  $\Delta$  remains constant. The pressure induced shift calculated in this fashion is -0.46 ppm/Kbar and is due almost completely to the change in  $\sigma^{\text{P}}$  since the  $\sigma_{\text{F}}^{\text{P}}$  is pressure independent and the contribution  $\sigma_{\text{overlap}}^{\text{d}}$  is estimated to be less than 0.01 ppm/Kbar.

Finally, it can be pointed out that the pressure induced shift calculated by using equation 10, derived from equation 7 using the previous approximation, differs from the result given above by less than 0.01 ppm/Kbar.

PROTON CHEMICAL SHIFT TENSORS

( Portions of the following text are from a paper coauthored with R. W. Vaughan that has been published in Chemical Physics Letters, Volume 1, Number 3, 1975.)

With the development of the multiple pulse NMR techniques<sup>(3-7)</sup> it has become possible to routinely measure proton magnetic shielding tensors. These chemical shift tensors contain information on electronic structure, or chemical bonding, within the materials studied, yet their interpretation in terms of the electronic wavefunctions and charge distributions within the materials being studied is complex and difficult. The theoretical basis for such an interpretation was initially formulated by Ramsey<sup>(8)</sup>,

$$\vec{\sigma}_{\lambda} = \vec{\sigma}_{\lambda d} + \vec{\sigma}_{\lambda p}, \quad (13)$$

where

$$\vec{\sigma}_{\lambda d} = \left( \frac{e^2}{2mc^2} \right) \langle n\lambda | \sum_{K=1}^N \frac{I^d(\vec{r}_k - \vec{R}_{k1}) \cdot \vec{r}_k - (\vec{r}_k - \vec{R}_{k1}) \vec{r}_k}{r_k^3} | n\lambda \rangle \quad (14)$$

$$\vec{\sigma}_{\lambda p} = -4 \text{Re} \sum_{n'} \frac{\langle n\lambda | \sum_{K=1}^N \vec{m}_{k0} / r_k^3 | n'\lambda \rangle \langle n'\lambda | \vec{m}_{k1} | n\lambda \rangle}{E_{n'} - E_n} \quad (15)$$

$$\vec{m}_{k1} = (ie\hbar/2mc)(\vec{r}_k - \vec{R}_{k1}) \times \vec{v}_k \quad (16)$$

$$\vec{m}_{k0} = (ie\hbar/2mc)\vec{r}_k \times \vec{v}_k \quad (17)$$

Ramsey's formulation separated the shielding tensor into two components, a diamagnetic term,  $\vec{\sigma}_d$ , which is calculated from ground state wavefunctions ( Equation 14), and a paramagnetic term,  $\vec{\sigma}_p$ , which involves a

summation over all excited states (Equation 15). As knowledge of the excited state wavefunctions is normally not available, exact calculation of the paramagnetic term is not possible, and although numerous approximate methods of estimating this term have been proposed<sup>(18-22)</sup> its evaluation remains a difficult problem. It is being proposed here that insight into the interpretation of the chemical shift tensor can be obtained by comparing the measured tensors with the results of a model calculation which can be easily performed and which has a straightforward physical interpretation.

#### GEOMETRICAL AND CHEMICAL CONTRIBUTIONS TO THE CHEMICAL SHIFT TENSOR

One can envision the formation of a molecule or solid to take place in two steps, (1) first bring together the atoms or ions such that the nuclei are in the proper positions relative to one another, not allowing the electrons to interact, and (2) then allowing the electrons to interact and relax into the proper molecular configuration. As it is in the second of these two steps that the electronic interaction associated with chemical bonding takes place it is convenient to refer to the changes in the chemical shift tensor due to this step as "chemical" in nature, while the resulting chemical shift tensor obtained by the bringing together of atoms in step one would be more appropriately referred to as "geometrical" or non-chemical in nature.

#### CALCULATION OF THE GEOMETRICAL TERM

It is possible to calculate accurately and easily the effects of the first step, i.e., the geometrical or non-chemical contribution to

the chemical shift, and as it is demonstrated below, this contribution is a large fraction of the total chemical shift tensor in protons. Thus, by comparing the calculated chemical shift tensor of the hypothetical state after the first step with the measured chemical shift tensor it is possible to determine the characteristics of the chemical shift tensor which are due to the geometrical arrangement of atoms or ions.

A spherical charge distribution, equal occupancy of the p orbitals, is assumed for the non-interacting ions or atoms in step one above, and Ramsey's formulation<sup>(8)</sup> is used to calculate the total chemical shift tensor. Referring to Equations 14&15,  $|n\lambda\rangle$  represents the ground state wavefunction expressed in coordinate system denoted by  $\lambda$ , while  $|n'\lambda\rangle$  represents the n'th excited state function;  $\vec{r}_k$  is the position of electron k from the nucleus of interest;  $\vec{R}_{k1}$  is a vector from the nuclei of interest to the location of the vector potential gauge center for the electron k; and  $I^d$  is the unit dyadic. Ramsey pointed out that for non-interacting systems of spherical symmetry one can chose  $\vec{R}_{k1}$  to be  $\vec{R}_K$  the vector from the nucleus of interest to the nucleus of the atom or ion containing electron k and make the paramagnetic contribution,  $\vec{\sigma}_{\lambda p}$ , vanish. Since the model is for non-interacting electrons between atoms or ions a simple product wavefunction can be used and it is appropriate to chose a separate vector potential for each atom or ion, and for a spherically symmetric entity centered at  $\vec{R}_k$  a choice of  $\vec{R}_{k1} = \vec{R}_K$  forces the sum over excited states to equal zero. Thus, one obtains the following expression for the full chemical shift tensor for the model system of non-interacting ions or atoms:

$$\vec{\sigma}_\lambda = \sum_K \vec{\sigma}_\lambda^K = \left( \frac{e^2}{2mc^2} \right) \sum_K \langle n_k \lambda | \sum_{k=1}^{N_k} \frac{I^d(\vec{r}_k - \vec{R}_K) \cdot \vec{r}_k - (\vec{r}_k - \vec{R}_K) \vec{r}_k}{r_k^3} | n_k \lambda \rangle. \quad (18)$$

This expression is easily evaluated given electronic ground state wavefunctions appropriate for the atoms or ions within the solid. As Equation 18 indicates, the total chemical shift tensor is a linear sum of the contributions from each atom or ion. Considering a single near-by ion or atom, J, one notes that the contribution to the chemical shift tensor from this source must, by symmetry, be axially symmetric around the vector  $R_J$ , between the nucleus of interest and the nucleus J. Thus, one needs only two components of the chemical shift tensor to characterize it fully,  $\sigma_{\parallel}$  the value parallel to  $R_J$ , and  $\sigma_{\perp}$  the value perpendicular to  $R_J$ . Assuming  $R_J$  is parallel to the z axis and of magnitude  $Z_J$  one obtains:

$$\sigma_{\parallel}^J = \sigma_{zz}^J = \frac{e^2}{2mc^2} \langle n_J \lambda | \sum_{k=1}^{N_J} \frac{x_k^2 + y_k^2}{r_k^3} | n_J \lambda \rangle, \quad (19)$$

$$\sigma_{\perp}^J = \sigma_{yy}^J = \sigma_{xx}^J = \frac{e^2}{2mc^2} \langle n_J \lambda | \sum_{k=1}^{N_J} \frac{x_k^2 + (z_k + Z_J)^2}{r_k^3} | n_J \lambda \rangle. \quad (20)$$

To include the effects of other atoms or ions one repeats the calculations for each, transform all the resulting tensor contributions to the same coordinate systems and sums them to obtain the total tensor.

In this fashion one can easily calculate the "geometrical" contribution to the chemical shift tensor even in highly complex geometries. It should be emphasized that these model calculations accurately represent the model situation as in this case one handles the paramagnetic term exactly and in legitimate fashion. The results

are gauge independent, and depend numerically only on the gross shape of the wavefunctions used, and consequently would not be expected to vary with the small variation in free atom, or ion, wavefunctions used as a basis for the calculation. These results can then be compared with experimentally measured tensors to determine the relative importance of this geometrical term.

#### A REFINED MODEL FOR THE INTERPRETATION OF THE CHEMICAL TERM

The nature of the remaining chemical term depends on the exact electronic structure of the solid and cannot be calculated as simply as the geometrical term. In fact, the purpose of the above separation is not to provide a method to calculate the total chemical shift. Instead, it points out the portion of the experimentally measured shift which is directly related to the "chemistry" so that more meaningful correlation between the measured tensor with the electronic structure can be made. Yet, it is worthwhile if a simple scheme can be devised which explains the behavior of the chemical term with the main features of the electronic wavefunction of the particular solid. To accomplish this, one would want a model which include some, or hopefully a major part of the chemical term. First, one digresses a bit to consider the physical origin of the chemical shift tensor.

Whenever an external magnetic field is applied to a sample, electric currents are induced around the nuclear spins. These induced currents in turn produce a secondary magnetic field at the nuclear site to cause chemical shift tensor. Macroscopic analogy of induced currents can be found by considering a perfectly conducting wire in a closed

loop and placed in a magnetic field. The turning on of the field generates an EMF which causes the current to flow in the constraint of the conducting wire. In this case the path of the electrons is determined by the geometry of the wire. In the atomic case, however, the "constraint" is the electric potential and does not determine the path of electrons in the same obvious manner as the macroscopic case. When the electric potential is axially symmetric as in the case of isolated atom it seems reasonable that the path of the electrons would be in a circle. Lamb's formula<sup>(31)</sup> for the atomic diamagnetic current is derived classically with this assumption. The vector gauge center can, in this case, be chosen to be at the center of the atom and the electric current is parallel to the vector potential at all points in space. Here classical derivation gives the correct current distribution because quantum mechanically there is no paramagnetic current. In molecules and solids neighbor atoms or ions distort the symmetry and the path of electron circulation is no longer easily determined. As a result the calculation of chemical shift becomes very complicated.

Because of the strong attractive centers of the positive charged nuclei, it is reasonable to assume that, to a first approximation, atoms and ions in the solid retain their wavefunction as in the isolated case and electrons circulate around their respective nuclei. This is the physical consideration that motivates the separation of the geometrical part from the total shift. Chemical bonding can alter this picture in several different ways. In metals and semiconductors some electrons are free to move among all centers in the solids. In aromatic compounds, for example, part of the electrons may circulate in the aromatic

rings. Even in solids in which electrons can be loosely considered as localized, the electronic charge can be redistributed and the states distorted by bonding effects.

In view of this physical consideration, the following refined model is proposed to attempt a more detailed description of the chemical shift in solids containing localized electrons. One notes that in the geometrical term the wavefunctions are that of isolated atoms or ions. Conceivably, they are not necessarily the best ones to be used. Considering first the effect of redistribution of electronic charges among the atoms, one can propose a description using similar spherical wavefunctions centered on each nucleus but with the orbitals containing different amount of electronic charges from the isolated atom case and the orbitals being contracted or expanded. Since the physical picture is analogous the same calculation with the same gauge choice can be applied. This type of induced current is referred to as the diamagnetic current because it is calculated from the diamagnetic part of the Ramsey's expression (although with a different gauge choice). The chemical term caused by the charge redistribution effect is, thus, the difference of the two calculations using the isolated atom wavefunctions and the modified wavefunctions.

The distortion of the isolated atom wavefunction caused by the non-axially symmetric potential can be described also by using atomic orbitals. In this case the orbitals are no longer assumed to be axially symmetric so that atomic excited states can mix in with the ground state to create a current circulating in the opposite direction from the diamagnetic current when the atom is placed in a magnetic field.

This type of calculation can best be illustrated by an example considered in reference 1, chapter 4. In that example one considers a p atomic orbital whose angular momentum is quenched by the crystalline field of the neighbor charge centers. When external magnetic field is applied the p electron produces a current and a chemical shift at the nuclear site of the same atom. This current flows in the opposite direction of the diamagnetic current and is found to circulate in a smaller circle with its magnitude depending on the excitation energy parameter. The gauge choice can be chosen to be the same as that used in the rest of the calculations and the current can be referred as paramagnetic current but with a specific choice of gauge.

In effect, this description of the chemical shift tensor assumes that, as far as the calculation of the induced current is concerned, the actual electronic wavefunction of the solid can be approximated by a superposition of atomic orbitals each centered at their respective nuclei. When external magnetic field is applied there exist on each atom a circulating diamagnetic current and a paramagnetic current in the opposite direction. The chemical shift is thus the combined effect of the induced field at the shielded nucleus due to all these current loops situated according to the crystal structure of the solid.

Rigorously, there is no unique way to breakdown the wavefunction of the actual solids as to achieve the above picture of the currents and this refined model of the chemical shift does not have the same theoretical footing as the geometrical term. In fact, in the widest sense it is like trying to fit the measured shift with numerous parameters associated with each current loop. In actual application,

using a L.C.A.O. type description of the wavefunction of solids, the behavior of the atomic wavefunction can be specified in a rather predetermined fashion. Therefore, complete arbitrariness of the description will not occur. In any case, atomic orbitals are rather "physical" concepts. To relate it to the chemical shift tensors is to provide a way to characterize electronic wavefunction by chemical shift measurements. A similar physical picture of the chemical shift has been described by Pople<sup>(32)</sup>. The difference lies in the way of emphasis. For example, gauge invariant orbitals were used in Pople's calculation whereas in the present interpretation regular atomic orbitals can be used because gauge has been specifically chosen. In the case of proton shift Pople treated the neighbor contribution by a dipole approximation, but in this interpretation the full current distribution of the neighbor atom is calculated. Pople's formulation emphasized the calculation of the isotropic part of the chemical shift tensor whereas in the present case the geometrical term is specifically separated out and the anisotropic nature of the proton chemical shift tensor is emphasized.

#### APPLICATION OF THE GEOMETRICAL TERM

In the following one considers first some examples of the use of geometrical term in the interpretation of the measured proton chemical shift tensors. As mentioned earlier the geometrical term can be calculated by considering atoms and ions individually. For the contribution to the chemical shift tensor from a spherical charge cloud a distance  $R_k$  away from the shielded proton one uses Equations 19 and 20. In terms of explicit integrals they can be written as:

$$\sigma_{\parallel k} = \frac{\alpha^2}{3} \left[ \frac{1}{R_k^3} \int_{r' < R_k} r'^2 \rho(r') d^3 r' + \int_{R_k < r'} \frac{\rho(r')}{r'} d^3 r' \right] \quad (21)$$

$$\sigma_{\perp k} = \frac{\alpha^2}{3} \left[ -\frac{1}{2R_k^3} \int_{r' < R_k} r'^2 \rho(r') d^3 r' + \int_{R_k < r'} \frac{\rho(r')}{r'} d^3 r' \right] \quad (22)$$

where  $R_k$  and  $r'$  are written in unit of bohr radius;  $\alpha$  is the fine structure constant;  $\rho(r')$  is the radial charge distribution of the electron cloud. One notes that these same equations had been derived in Lamb's paper<sup>(31)</sup> for a slightly different purpose.

In the case of proton chemical shift the contribution from the 1 s orbital electron at the same proton can be easily obtained to be  $\sigma_{\parallel} = \sigma_{\perp} = 17.75$  ppm, using free hydrogen wavefunction. For other atoms and ions nearby, their contributions to the proton shift, in the isolated atom approximation, can be calculated from Equations 21 and 22 using Clementi's Hartree Fock free ion wavefunctions<sup>(28)</sup>. The result of several different atoms and ions is shown in Figures 3a and 4. One notes that the neighbor contribution is very sensitive to change in  $R_k$  and for a typical distance (2 bohr radii) between the proton and its neighbor atom the neighbor can contribute large anisotropy ( $\sim 20$ ppm) to the proton shift. In general the neighbor acts as a magnetic dipole at large  $R_k$ 's but as  $R_k$  decreases this dipole approximation breaks down and as the proton gradually goes "inside" the neighbor,  $\sigma_{\perp}$  eventually becomes positive. In such case the neighbor contributes not only to the anisotropic part of the proton shift tensor but also to the isotropic part. One important characteristic of this type of contribution is that it is not sensitive to the kind of nuclei nearby except, roughly speaking, it increases as the number of electrons or the size of the nearby neighbor increases.

Most of the recently reported data on proton chemical shift tensors (4,33-37) has dealt with the hydrogen bonded hydroxyl protons, and this system is analyzed below by comparing the model calculations with the experimentally measured tensors to illustrate that in this case the geometrical term accounts for the qualitative shape and orientation of the tensor.

Six quantities are needed to specify the chemical shift tensor. Normally three principal values and the three angles orienting the principal axis system within the molecular frame of reference are given. For the case of a linear hydrogen bonded system, O-H...O, the model calculation indicates that the principal axis frame has one axis parallel to the O-H...O crystallographic direction, and that the tensor is axially symmetric around this principal axis.

Thus, two of the principal values are predicted to be equal and they are the two that are perpendicular to the O-H bond direction. Measurement of the absolute values of components of the chemical shift tensor have not been reported and therefore the numerical results of solutions of Equations 21 and 22 are presented in Figure 1b where the total asymmetry for the O-H...O system is plotted for a typical O-O separation of  $2.7 \text{ \AA}$  ( $\approx 5.1$  bohr radii) and as a function of the O-H separation. Thus one predicts anisotropies from the "geometrical effect" of  $+28 \rightarrow +40$  ppm depending upon the O-H separation and with the O-H bond direction being the most shielded direction.

In all cases where data have been reported the chemical shift tensors for protons in hydroxyl groups have been found to be nearly axially symmetric with the unique principal value being directed along the O-H

bond direction and that principal value has always been the most shielded component of the tensor. Specifically, reported values of anisotropies,  $\sigma_{\parallel} - \sigma_{\perp}$ , are: +22.6, +19 ppm (maleic acid<sup>(34)</sup>), +19 ppm (malonic acid<sup>(33)</sup>), +17 ppm (oxalic acid<sup>(35)</sup>), +20 ppm ( $\text{MgSO}_4 \cdot \text{H}_2\text{O}$ <sup>(36)</sup>), +20 ppm (trichloroacetic acid<sup>(4)</sup>) and +21.6 ppm (gypsum<sup>(37)</sup>). For the last two values detailed calculations of the geometrical terms are possible because the structure information is available (see Table II). Thus, the geometrical term is found to predict the general form or shape of all the measured tensors, and in fact, only differs from the measured values in predicting anisotropies that are slightly too large. A few other proton chemical shift tensors are also measured. In Table II the measured anisotropies in  $\text{KHF}_2$  and  $\text{Ca(OH)}_2$  are also compared with the anisotropies predicted by the geometrical term. The result shows that in  $\text{KHF}_2$  the geometrical term predicts the correct anisotropy suggesting little chemical effects while for the  $\text{Ca(OH)}_2$  the disagreement is larger suggesting larger chemical effects than those of the hydroxyl proton. In other kind of proton such as the olefinic proton in the maleic acid<sup>(34)</sup> both the direction and anisotropy disagree, signifying even larger chemical effects.

Incidentally, one notes that the main portion of the total anisotropy in the geometrical term comes from the O-H group or the O-H...O group. For example, the geometrical term of the trichloroacetic acid crystal, taking into account all atoms within 7 bohr radii of the proton, gives  $\Delta\sigma = 37.5$  ppm while taking the O-H...O group alone gives  $\Delta\sigma = 34.0$  ppm (inclusion of the atoms other than the O-H...O group also changes the direction of the principal axis slightly but not significantly).

For the case of  $\text{Ca}(\text{OH})_2$ , anisotropy predicted by the geometrical term is 35.7 ppm, including ions within 7 bohr radii of the proton. The contribution from the  $\text{O}^-$ -H group alone is 35.6 ppm. The fast convergence of the geometrical term for far away atoms or ions makes this theory superior to the atom dipole method by Flygare<sup>(38)</sup>. In the atom dipole method the molecule is approximated by atomic charge distribution but a single gauge is chosen at the proton site for all the electrons. As a result the contributions from far away atoms or ions do not converge. In addition, the atom dipole method is technically valid only for small molecules because it requires the spin rotation constant to account for the paramagnetic part and the spin rotation constant is available only for small molecules.

Recent papers on proton chemical shift tensor measurement have used the atom dipole method to interpret their results<sup>(33,34)</sup>. It is felt that the present scheme should be used instead, for it not only is simpler numerically but also has better physical meaning.

#### APPLICATION OF THE REFINED MODEL

It seems, from the above comparison, that the anisotropy predicted by the geometrical term tends to be larger than the the actual observed result. The reason can be attributed to the paramagnetic current as discussed in the refined model. In calculating the shift due to the paramagnetic current on the heavy atom bonded to the proton, instead of finding the shift at the nucleus of the same atom as mentioned previously, it is possible to calculate its effect on the shielding of the nearby proton. The important characteristic of this type of contribution to

the proton shift is that the paramagnetic current on this neighbor atom is dependent on the orientation of the solid in the external magnetic field because the wavefunction is not spherical symmetric and the excitation energy parameter is not necessarily isotropic. In the isolated H-atom case, for example, the paramagnetic current on the atom is identically zero when the external field is parallel to the H-atom axis but is of finite value when they are perpendicular. Of course there will also be paramagnetic current on the hydrogen atom, but it is expected to be small because only 1 s electron is important in the hydrogen atom. One notes that this anisotropy of the paramagnetic current strength as a function of orientation can contribute much to the isotropic part of the proton chemical shift tensor as well as the anisotropic part. Furthermore, since the paramagnetic current is in the opposite direction, the anisotropic contributions from diamagnetic and paramagnetic currents tend to cancel one another. This explains why the geometrical term predicts too large an anisotropy. The fact that  $\pi$  bond has larger paramagnetic current effect so as to affect the olefinic proton in maleic acid is not surprising. It has been shown by an atomic orbital calculation found in Pople's paper<sup>(32)</sup>.

#### COMPARISON WITH OTHER CALCULATION OF PROTON CHEMICAL SHIFT TENSORS

Starting with the simple case of  $H_2$  molecule, the result of the present model can be compared with the result of more elaborate calculations<sup>(39)</sup>. The proton chemical shift tensor in  $H_2$  is expected from the symmetry of the molecule to be axially symmetric and can be described by two parameters  $\sigma_{\parallel}$  and  $\sigma_{\perp}$  corresponding respectively to the

principal axis of the tensor along the H-H bond and perpendicular to it. In the other calculation<sup>(39)</sup> they are calculated to be  $\sigma_{\parallel} = 28.18$  ppm and  $\sigma_{\perp} = 25.95$  ppm for the equilibrium distance (1.4 bohr radii) between the protons. The geometrical contribution reflects the same symmetry and gives  $\sigma_{\parallel} = 24.8$  ppm and  $\sigma_{\perp} = 20.36$  ppm. If the orbital exponent of the hydrogen 1 s orbital is changed to 1.2 similar to that used in the other calculation the result is  $\sigma_{\parallel} = 27.9$  ppm and  $\sigma_{\perp} = 22.9$  ppm. This suggests that for the type of bonding in  $H_2$  molecules the free atom approximation, i.e. the geometrical term, describes the shift quite well and better result can be obtained by simply contracting the 1 s orbital. The remaining error is small and the present model relates the proton shift with the type of bonding in  $H_2$  molecule satisfactorily in a rather simple manner.

For several small molecules containing proton, Ditchfield has performed ab-initio calculations<sup>(40)</sup>. In Table III the geometrical term is compared with his calculation. This comparison again shows that the geometrical term is a large part of the calculated shift and predicts the same qualitative nature. In general, the component of the proton shift tensor perpendicular to the H-atom axis predicted by the geometrical term is smaller. If one assumes that Ditchfield's calculation approaches the true shift better this comparison means that the interpretation of a paramagnetic current on the heavy atom is essentially correct and that for these molecules the paramagnetic current on the near neighbor atom of the proton is substantial and reduces the anisotropy predicted by the geometrical term. The isotropic part of the chemical shift tensor is affected by both contributions, geometrical

and chemical. Neglecting either one of them would lead to wrong predictions. Again, the  $\pi$  bond (in ethylene and formaldehyde) appears to have the largest effect. In fact, the principal axis system of the proton chemical shift tensor as calculated otherwise seems to be influenced more by the  $\pi$  bonding than the geometrical term.

#### POTENTIAL APPLICATION OF THE REFINED MODEL

A more detailed analysis of the experimentally measured proton chemical shift tensor is possible if the absolute shift can be established. The following absolute shifts are obtained by comparing the relative shifts of many compounds with the absolute shift of the  $H_2$  gas (26.6 ppm). The results are only approximate values because susceptibility correction has not been in all cases properly performed. The absolute shift of protons in  $Ca(OH)_2$  is estimated to be  $\sigma_{\parallel} = 40$  ppm and  $\sigma_{\perp} = 28$  ppm. The geometrical term gives  $\sigma_{\parallel} = 62.05$  ppm and  $\sigma_{\perp} = 26.35$  ppm. The chemical term is, therefore,  $\sigma_{\parallel c} = -22.05$  ppm and  $\sigma_{\perp c} = 1.65$  ppm. Presumably, the main portion of the chemical term is a combination of two effects: the charge redistribution and the paramagnetic current on the oxygen. Exactly how important is one term relative to the other is not known without more detailed knowledge of the "correct" atomic orbitals. In any case the paramagnetic current when the magnetic field is parallel to the O-H bond cannot be small which means that to consider O-H as isolated unit in the solid and predict that the paramagnetic current is small is unwarranted. For the trichloroacetic acid the absolute shift suggested by experiment and deduced by the above method is  $\sigma_{\parallel} = 33$  ppm and  $\sigma_{\perp} = 12$  ppm while the geometrical term gives

$\sigma_{\parallel} = 49.55$  ppm and  $\sigma_{\perp} = 12.05$  ppm. In order to account for the small  $\sigma_{\perp}$  some local paramagnetic current may have to be allowed on the proton when the magnetic field is perpendicular to the O-H bond. This may suggest a p orbital on the proton directed along the O-H bond and there may be an electronic "bridge" linking the two oxygen atoms in the formation of the hydrogen bond.

The above examples have not been discussed in detail but serve mainly to indicate how this model can be applied to interpret proton chemical shift tensors in the future when more data on different systems and more knowledge about the different wavefunctions as described by atomic orbitals are available to allow better characterization of the concepts involved in this model. A useful experiment would be to measure the chemical shift on the heavy nucleus next to the proton. This measurement should furnish information on the paramagnetic current on the heavy atom directly because other factors are relatively unimportant. As these concepts of the present model are developed, one can use them to predict wavefunctions in unknown materials by measurement of chemical shift tensor. Hopefully such scheme can help the understanding of more complex systems such as surfaces and biological systems.

CONCLUSION

Measurement of chemical shift tensors in solids is now a fairly routine operation with the development of multiple pulse techniques. The 8 pulse cycle is, among the different pulse cycles, relatively stable and can be adopted to be used in measurements under various conditions, including the high pressure condition.

The pressure dependence of a low atomic weight species,  $^{19}\text{F}$  has been measured in  $\text{CaF}_2$  and found to be  $-1.7 \pm 1$  ppm/Kbar, while a calculation using wavefunctions obtained with the symmetrical orthogonalization techniques of Löwdin<sup>(25)</sup> and using the overlap model of Kondo-Yamashita<sup>(14)</sup> predicts a value of  $-0.46$  ppm/Kbar. The calculation contains no adjustable parameters and succeeds in predicting a pressure induced shift in the proper direction and within a factor of three of the proper magnitude.

The localized theory which considers only the electrons on the shielded nucleus is not adequate to account for the proton shifts. A conceptually simple and physically meaningful way to interpret the proton shift is proposed. The main conclusion from this interpretation is that geometrical contribution is a large portion of the total measured proton shift tensors. The contribution which results from the complex electronic interactions involved in the chemical bond formation is to be obtained by subtracting this large geometrical contribution from the measured proton tensor. The separation into geometrical and chemical terms is probably useful only in the proton shift because the shifts of the heavy nuclei are much larger and the neighbor geometrical terms are much smaller due to longer interatomic distances.

REFERENCE

1. C. P. Slichter, Principles of Magnetic Resonance (Harper and Row, 1963).
2. J. A. Pople, W. G. Schneider and H. J. Bernstein, High-resolution Nuclear Magnetic Resonance (McGraw-Hill, 1959).
3. J. S. Waugh, L. M. Huber and U. Haeberlen, Phys. Rev. Lett. 20, 180 (1968); U. Haeberlen and J. S. Waugh, Phys. Rev. 175, 453 (1968).
4. W.-K. Rhim, D. D. Elleman and R. W. Vaughan, J. Chem. Phys. 58, 1772 (1973); 59, 3740 (1973).
5. W.-K. Rhim, D. D. Elleman, L. B. Schreiber and R. W. Vaughan, J. Chem. Phys. 60, 4595 (1974).
6. P. Mansfield, J. Phys. C4, 1444 (1971).
7. R. W. Vaughan, in: Annual Reviews in Material Science, Vol. 4, eds. R. A. Huggins, R. H. Bube and R. W. Roberts (Annual Reviews, Palo Alto, 1974), and references therein.
8. N. F. Ramsey, Phys. Rev. 86, 243 (1952); 78, 699 (1950); 77, 567 (1950).
9. A. Saika and C. P. Slichter, J. Chem. Phys. 22, 26 (1954).
10. M. Karplus and T. P. Das, J. Chem. Phys. 34, 1863 (1961); M. Karplus and J. A. Pople, J. Chem. Phys. 38, 2803 (1963).
11. N. Bloembergen and P. P. Sorokin, Phys. Rev. 110, 865 (1958).
12. R. W. Vaughan, et al., J. Chem. Phys. 57, 5383 (1972).
13. R. Baron, J. Chem. Phys. 38, 173 (1963).
14. J. Kondo and J. Yamashita, J. Phys. Chem. solids 10, 245 (1959).
15. G. B. Benedek, Magnetic Resonance at High Pressure (Interscience, New York, 1963).
16. J. H. Van Vleck and A. Frank, Proc. Natl. Acad. Sci. U. S. 15, 539 (1929).
17. A. D. McLachlan, J. Chem. Phys. 32, 1263 (1960).
18. D. E. O'Reilly, Progress in Nuclear Magnetic Resonance Spectroscopy, ed. J. W. Emsley, J. Freney, and L. H. Sutcliffe (Pergamon, London, 1967), Vol. II, P. 1.

19. Jeremy I. Musher, Advances in Magnetic Resonance, ed. J. S. Waugh (Academic, New York, 1966), Vol. II, p.177.
20. W. N. Lipscomb, Advances in Magnetic Resonance, ed. J. S. Waugh (Academic, New York, 1966), Vol. II, p.138.
21. J. W. Emsley and L. Phillips, Progress in Nuclear Magnetic Resonance Spectroscopy, ed. J. W. Emsley, J. Feeney, and L. H. Sutcliffe (Pergamon, Oxford, 1971), Vol. VII, p. 1.
22. R. Ditchfield, *J. Chem. Phys.* 56, 5688 (1972); S. I. Chan and A. S. Dubin, *ibid* 46, 1745 (1967).
23. D. Ikenberry and T. P. Das, *J. Chem. Phys.* 43, 2199 (1965).
24. D. W. Hafemeister and W.H. Flygare, *J. Chem. Phys.* 44, 3584 (1966).
25. P. O. Löwdin, *Advan. Phy.* 5, 1 (1956).
26. A. Saika and C. P. Slichter, *J. Chem. Phys.* 22, 26 (1954).
27. P. W. Bridgman, *Proc. Am. Acad. Art. Sci.* 77, 187 (1949).
28. E. Clementi, *IBM J. Res. Develop.* 9, 2 (1965). Suppl.
29. D. K. Hindermann and C. D. Cornwell, *J. Chem. Phys.* 48, 4148 (1968).
30. C. H. Dungan and J. R. Van Wagen, Compilation of Reported F<sup>19</sup> NMR Chemical Shifts (Wiley, New York, 1970), Appendix I.
31. W. E. Lamb Jr., *Phys. Rev.* 60, 817 (1941).
32. J. A. Pople, *Proc. Roy. Soc. (London)* A239, 541 (1957).
33. U. Haeberlen, U. Kohlschütter, J. Kempf, H.W. Spiess and H. Zimmermann, *Chem. Phys.* 3, 248 (1974).
34. R. Grosescu, A. M. Achlama (Chmelnick), U. Haeberlen and H. W. Spiess, *Chem. Phys.* 5, 119 (1974).
35. P. Van Hecke, J. C. Weaver, B. L. Neff and J. S. Waugh, *J. Chem. Phys.* 60, 1668 (1974)
36. U. Haubenreisser and B. Schnable, *Proc. of the 1st Specialized Colloque Ampère, Krakow, Poland* p.140 (1973).
37. C. M. Mcknett, C.R. Dybowski, and R. W. Vaughan, *J. Chem. Phys.* 63, 4578 (1975).
38. T. D. Gierke and W. H. Flygare, *J. Am. Chem. Soc.* 94, 7277 (1972).
39. D. B. Cook, A. M. Davis, and W. T. Raynes, *Mol. Phys.* 21, 113 (1971).

40. R. Ditchfield, Chem. Phys. 2, 400 (1973).
41. P. Van Hecke, H. W. Spiess and U. Haeberlen, J. Magnetic Resonance, ( to be published ).
42. L. B. Schreiber and R. W. Vaughan, Chem. Phys. Letters 28, 586 (1974).
43. W. G. Wyckoff, Crystal Structures (Interscience Publishers, 2nd ed.).
44. P. G. Jönsson and W. C. Hamilton, J. Chem. Phys. 56, 4433 (1972).
45. W. F. Cole and C. J. Lancucki, Nature (London) Phys. Sci. 242, 104 (1973).
46. L. C. Snyder and H. Basch, Molecular Wavefunctions and Properties, (Wiley Interscience, New York, 1972).

Table I. One- and two-center integrals for the paramagnetic shift calculation.

One-center integral		$\langle \phi_{0y}   \frac{1}{r_0}   \phi_{0y} \rangle_F = 6.3968$	
Two-center integrals			
Pressure		Atmospheric	10 Kbar
F-F Distance	(Bohr radius)	5.1617	5.1420
F <sup>-</sup> - F <sup>-</sup> Overlap Integrals	$S_{Oj}^{\sigma s}$	$4.52 \times 10^{-2}$	$4.59 \times 10^{-2}$
	$S_{Oj}^{\sigma \sigma}$	$-7.54 \times 10^{-2}$	$-7.61 \times 10^{-2}$
	$S_{Oj}^{\pi \pi}$	$2.52 \times 10^{-2}$	$2.56 \times 10^{-2}$
	$\langle \phi_{0\sigma}   \frac{1}{r_0}   \phi_{j s} \rangle$	$2.64 \times 10^{-3}$	$2.72 \times 10^{-3}$
	$\langle \phi_{0\sigma}   \frac{1}{r_0}   \phi_{j \sigma} \rangle$	$-1.81 \times 10^{-2}$	$-1.84 \times 10^{-2}$
	$\langle \phi_{0\pi}   \frac{1}{r_0}   \phi_{j \pi} \rangle$	$4.20 \times 10^{-3}$	$4.29 \times 10^{-3}$
F-Ca Distance		4.4702	4.4531
F <sup>-</sup> - Ca <sup>++</sup> Overlap Integrals	$S_{Oj}^{\sigma s}$	$7.38 \times 10^{-2}$	$7.47 \times 10^{-2}$
	$S_{Oj}^{\sigma \sigma}$	$-7.94 \times 10^{-2}$	$-8.04 \times 10^{-2}$
	$S_{Oj}^{\pi \pi}$	$-1.01 \times 10^{-4}$	$-1.03 \times 10^{-4}$
	$\langle \phi_{0\sigma}   \frac{1}{r_0}   \phi_{j s} \rangle$	$4.52 \times 10^{-3}$	$4.67 \times 10^{-3}$
	$\langle \phi_{0\sigma}   \frac{1}{r_0}   \phi_{j \sigma} \rangle$	$-1.41 \times 10^{-2}$	$-1.45 \times 10^{-2}$
	$\langle \phi_{0\pi}   \frac{1}{r_0}   \phi_{j \pi} \rangle$	$-1.20 \times 10^{-6}$	$-1.24 \times 10^{-6}$

TABLE II

Comparison between the Measured Proton Chemical Shift Anisotropy ( $\Delta\sigma$ ) and the Anisotropy obtained from the Geometrical Term Calculation

Solids	Measured $\Delta\sigma^a$ (in ppm)	Reference	Calculated $\Delta\sigma$ (in ppm)	Atoms (ion) Considered in Calculation	Crystal Structure Reference
KHF <sub>2</sub>	44.8 ± 1.0	41	40.5 48.5	F-H-F F <sup>-</sup> -H-F <sup>-</sup>	41
Ca(OH) <sub>2</sub>	14.0 ± 1.0	42	33.5 35.6	O-H O <sup>-</sup> -H	43
CCl <sub>3</sub> COOH	~20	4	34.0 40.0	O-H...O O <sup>-</sup> -H...O <sup>-</sup>	44
CaSO <sub>4</sub> ·2H <sub>2</sub> O	21.6 ± 1.0	37	33.6 <sup>b</sup> 39.2 <sup>b</sup>	O-H...O O <sup>-</sup> -H...O <sup>-</sup>	45

a.  $\Delta\sigma = \sigma_{zz} - \frac{\sigma_{xx} + \sigma_{yy}}{2}$  with the H-atom axis along the z direction

b. Averaged value of the 2 inequivalent protons whose calculated  $\Delta\sigma$ 's differ by < 0.5 ppm

TABLE III

Comparison Between the Geometrical Term and Ditchfield's Calculation of Proton Chemical Shift Tensors in Several Small Molecules

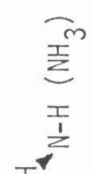
Molecule <sup>a</sup>	Geometrical Term <sup>b,c</sup>			Ditchfield's Calculation <sup>40</sup>				
	$\sigma_{xx}$	$\sigma_{yy}$ (ppm)	$\sigma_{zz}$	$\phi^d$ (deg.)	$\sigma_{xx}$	$\sigma_{yy}$ (ppm)	$\sigma_{zz}$	$\phi$ (deg.)
F-H	14.18	14.18	45.10	0	24.10	24.10	43.25	0
H-C=C-H	18.03	18.03	40.61	0	26.84	26.84	40.97	0
N=C-H	18.05	18.05	39.71	0	25.14	25.14	39.33	0
	17.95	17.95	38.02	0	29.69	29.69	39.11	0
	16.88	17.47	41.36	2.5	27.86	29.14	43.78	6.48
	16.33	15.47	43.84	2.3	27.32	25.77	44.10	5.50
	18.94	16.11	38.11	7.0	28.24	27.48	25.43	55.74

TABLE III (Continued)

Molecule <sup>a</sup>	Geometrical Term <sup>b,c</sup>			Ditchfield's Calculation <sup>40</sup>				
	$\sigma_{xx}$	$\sigma_{yy}$	$\sigma_{zz}$	$\phi^d$	$\sigma_{xx}$	$\sigma_{yy}$	$\sigma_{zz}$	$\phi$
	18.21	19.00	38.03	4.5	21.08	24.70	21.24	52.17
	19.10	16.89	38.61	7.5	30.98	27.99	38.29	15.33
	19.05	17.17	38.38	4.0	29.40	25.99	33.66	26.90
	18.71	17.31	38.43	4.5	29.72	25.63	32.19	33.90

a The shielding is in the Atom-H bond coordinate system,  $\sigma_{zz}$  is the component along the atom-H bond axis,  $\sigma_{yy}$  is the component perpendicular to the atom-H bond and the paper.

b Molecular geometry is taken from reference 46.

c Atomic wavefunction is taken from reference 28.

d  $\phi$  is the angle between the principal axis system and the coordinate system of a.

FIGURE CAPTIONS

- Fig. 1. Effect of pressure on the  $^{19}\text{F}$  chemical shift in  $\text{CaF}_2$ . Chemical shift values are relative to a  $\text{C}_6\text{F}_6$  reference.
- Fig. 2. Relative positions of the fluorine and calcium ions involved in the overlap calculation. The chemical shift of the  $^{19}\text{F}$  at the center fluorine ion is evaluated.
- Fig. 3. "Geometrical" contribution to proton chemical shift from (a) a single nearby atom, and (b) within a linear  $\text{O}-\text{H}\dots\text{O}$  arrangement with an  $\text{O}-\text{O}$  distance of  $2.70 \text{ \AA}$  (5.1 bohr radii). (i) is a typical hydrogen bonded proton  $\text{O}-\text{H}$  distance,  $1.01 \text{ \AA}$ , and (ii) is a typical non-hydrogen bonded hydroxyl  $\text{O}-\text{H}$  distance,  $0.79 \text{ \AA}$ .
- Fig. 4. "Geometrical" contribution to proton chemical shift from a single nearby atom as a function of the H-atom (or H-ion) distance.

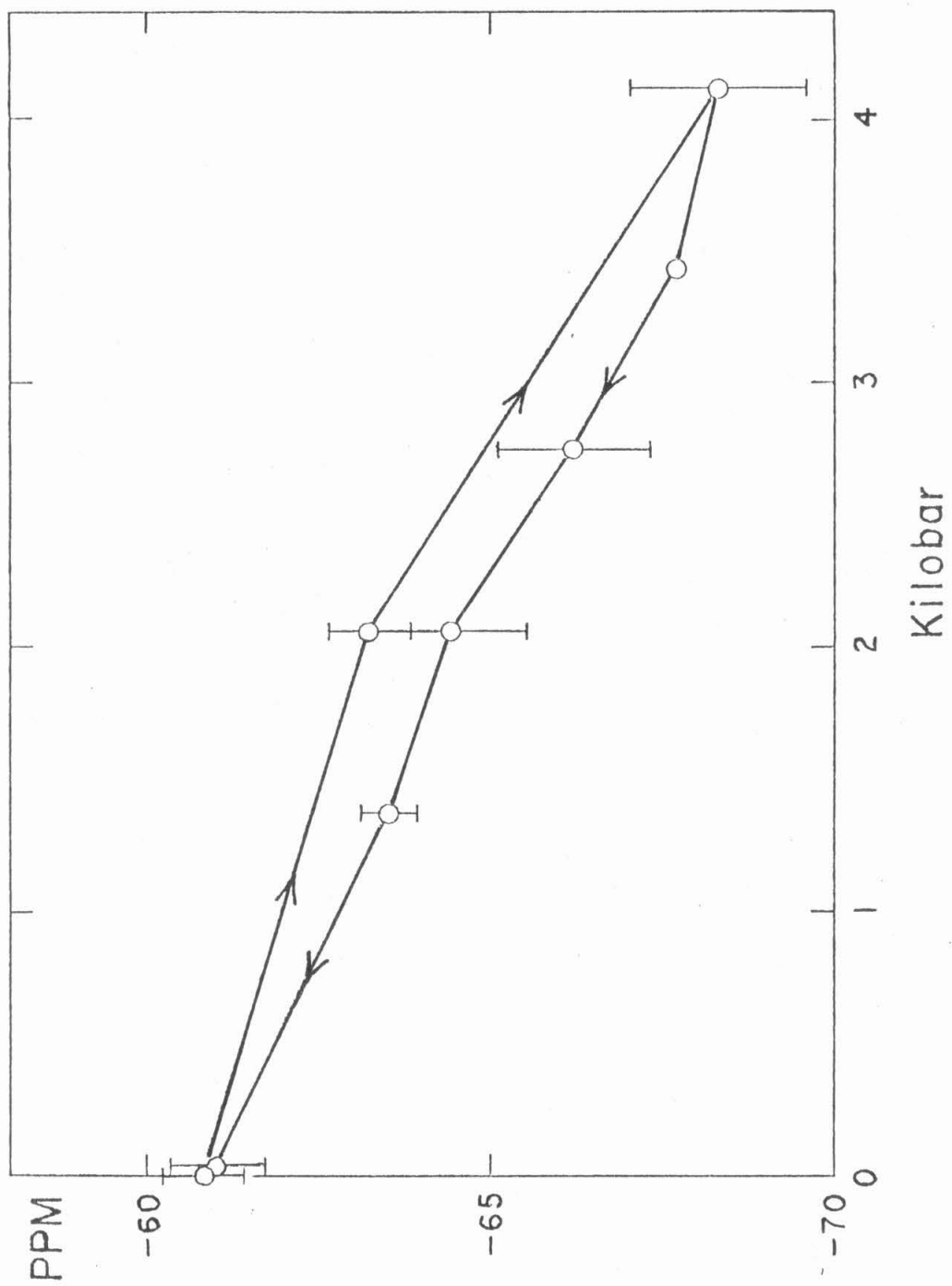


Fig. 1.

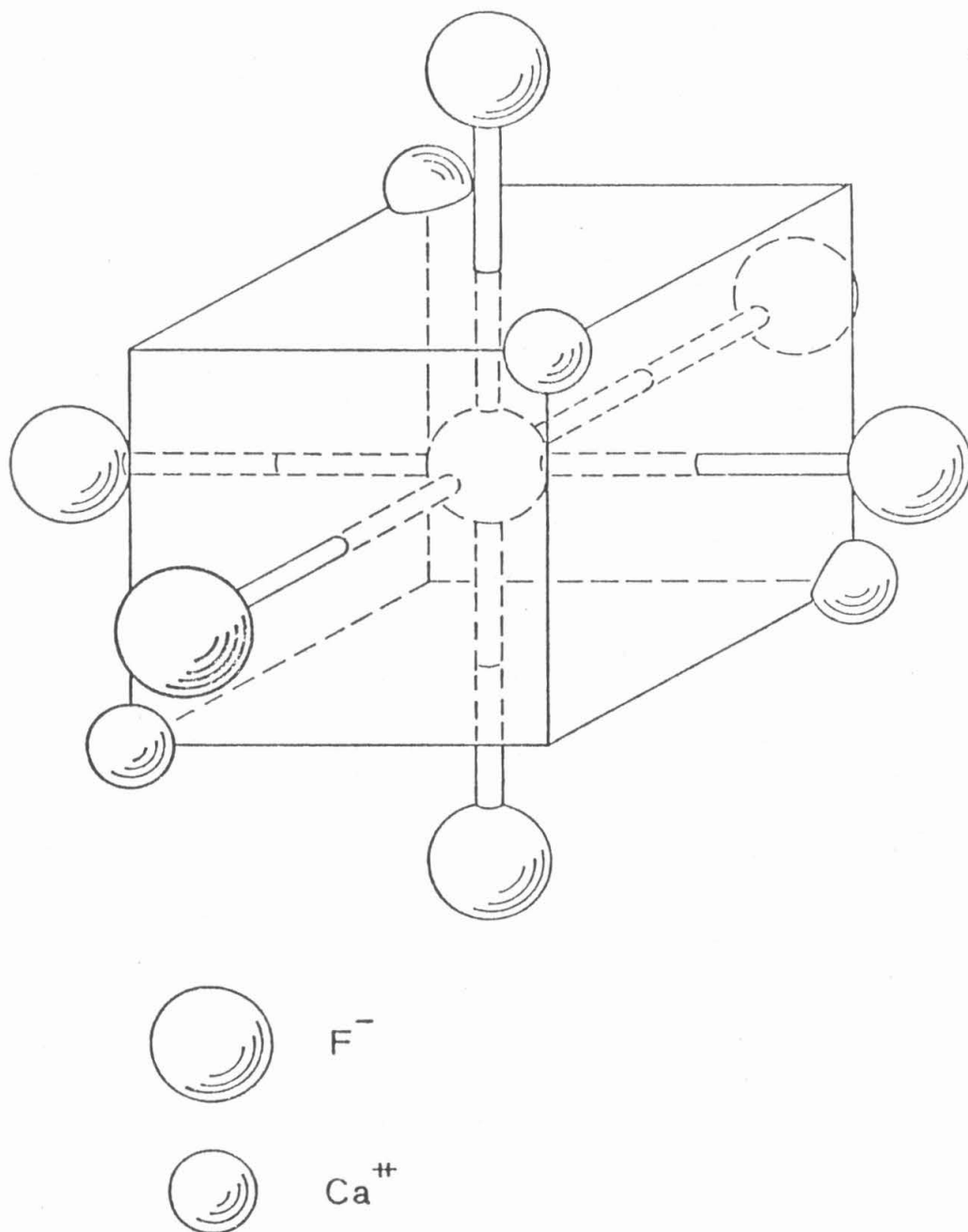


Fig. 2.

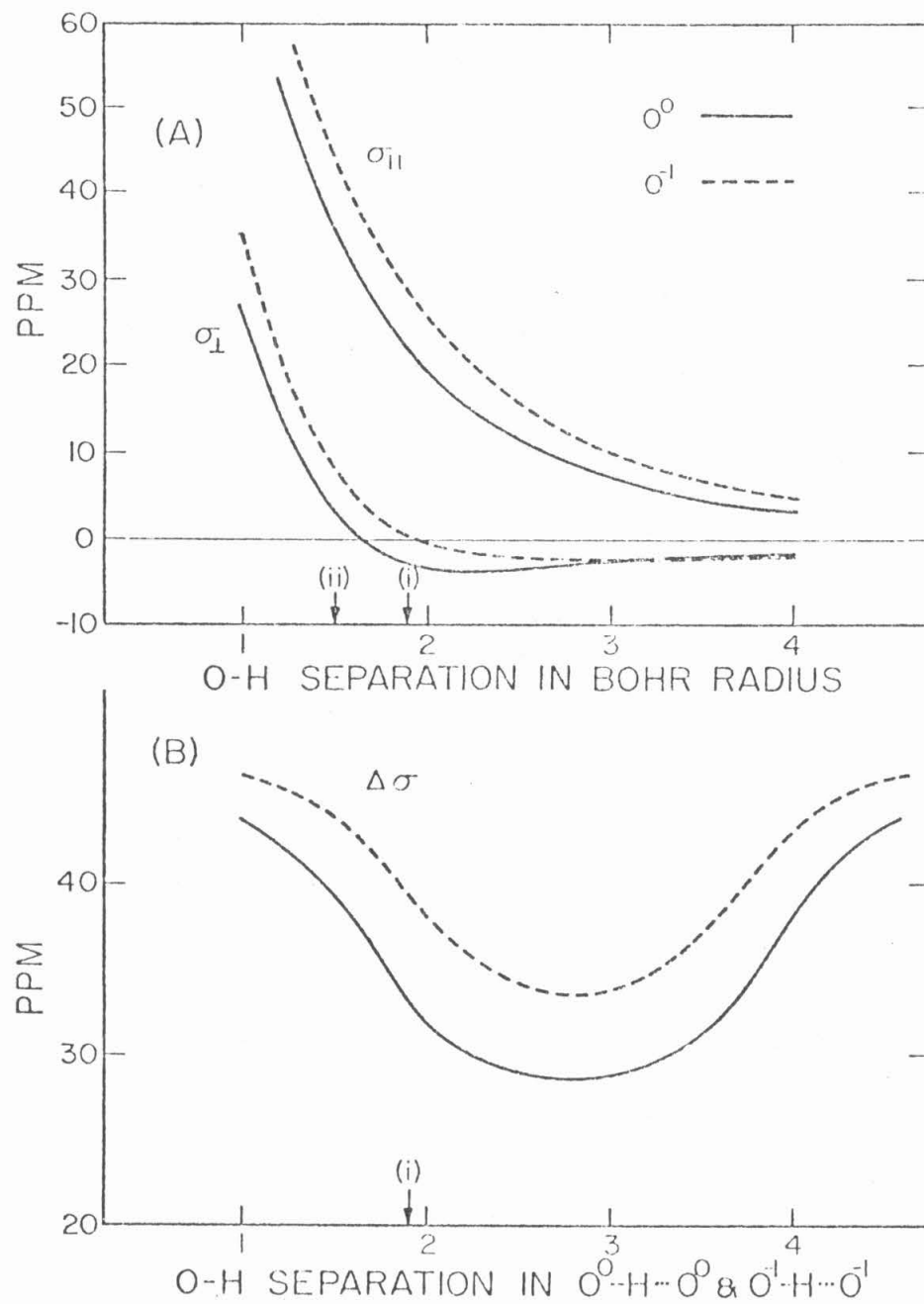


Fig. 3.

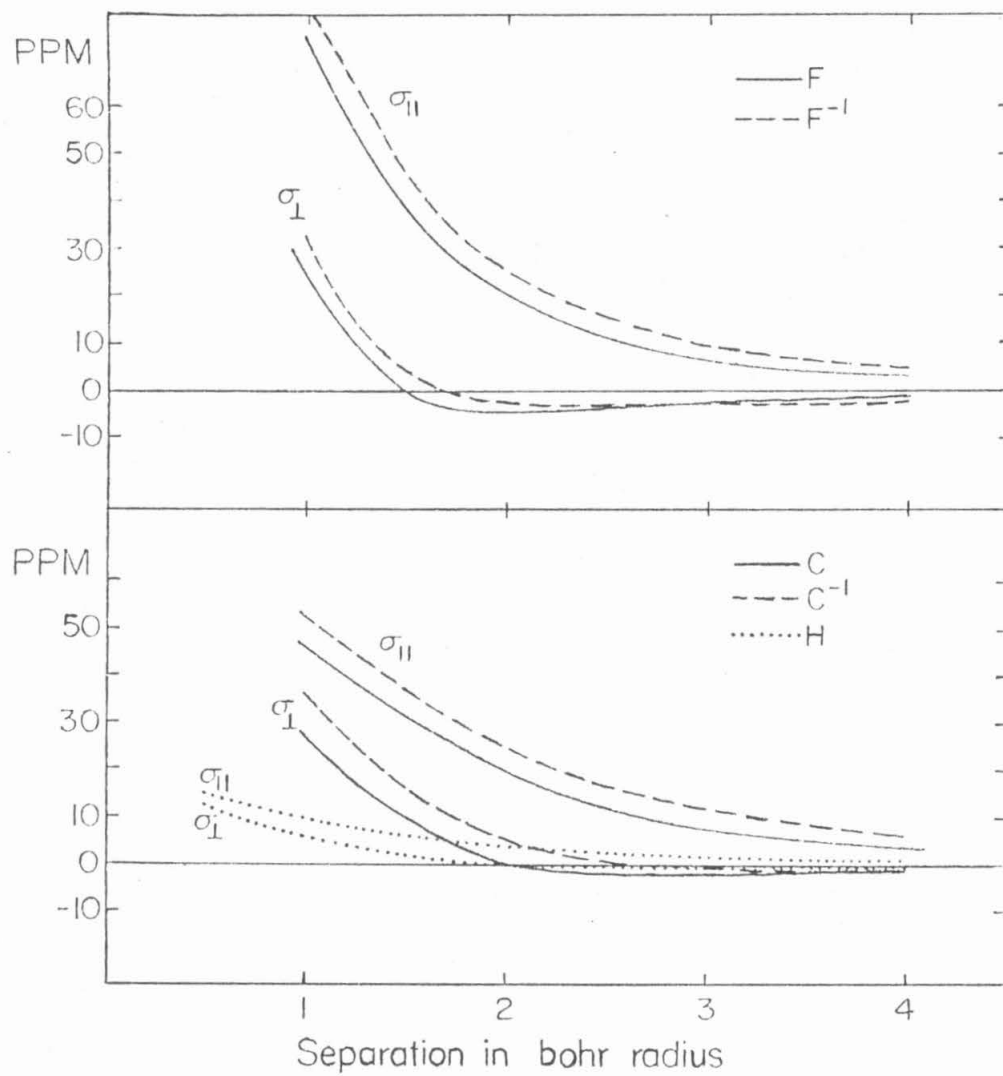


Fig. 4.

CHAPTER 3  
FLUORIDE ION MOTION IN DOPED  $\beta$ -PbF<sub>2</sub>

(The text of chapter 3 consists of an article coauthored with T. Y. Hwang, I. J. Lowe and R. W. Vaughan that has been submitted for publication in Journal of Chemical Physics. Both samples in this work were prepared by Lowe's group at University of Pittsburgh. Data of sample A are due to T. Y. Hwang and I. J. Lowe.)

## INTRODUCTION

Fluoride ion mobility in the cubic  $\beta$  phase of  $\text{PbF}_2$  has been the subject of numerous recent publications, both direct NMR studies of fluorine mobility<sup>(1-3)</sup> and measurements of electrical conductivity<sup>(3-10)</sup>. The occurrence of substantial ionic motion within this material many hundreds of degrees below its melting temperature has been demonstrated, and a further enhancement of fluoride ion motion has been shown recently to take place when a monovalent dopant, NaF, or KF is added to the crystal<sup>(2, 10)</sup>. This paper presents the results of further NMR measurements of the relaxation time constants  $T_1$ ,  $T_{1r}$  and  $T_2$  of NaF-doped  $\beta$ - $\text{PbF}_2$ . The parameters  $T_1$ ,  $T_{1r}$  and  $T_2$  were measured as a function of temperature,  $T_1$  and  $T_{1r}$  as a function of resonant frequency, and  $T_1$  and  $T_2$  as a function of pressure.

## EXPERIMENTAL DETAILS

Two  $\text{PbF}_2$  single crystals were studied and are denoted by A and B. They were grown from the melt as previously described<sup>(2)</sup>, and A contained 0.02% and B contained 0.12% by weight of NaF as a dopant. Chemical compositions were determined by spectroscopic analysis and are believed accurate to 10-20% of the reported values. The only other impurity found in any quantity in these crystals was vanadium (0.028% in crystal A sample and 0.01% in crystal B); this is suspected to be due to vanadium impurities in the graphite crucible used in

growth of the crystals.

The pulsed NMR spectrometers used for the measurements operated at 32 MHz<sup>(11)</sup> and 56.4 MHz<sup>(12)</sup> have been described previously.  $T_1$  was measured using a  $180^\circ$ - $\tau$ - $90^\circ$  pulse sequence or a  $90^\circ$ - $\tau$ - $90^\circ$  pulse sequence (relaxation curves were found to be exponential).  $T_2$  was defined as the time necessary for the free induction decay (fid) to fall to  $1/e$  of its initial value. The fid's were measured to be exponential with moderate motional narrowing.

The high pressure cell was of the Benedek design<sup>(13)</sup> and capable of pressures in the 10-kilobar range. A hydrocarbon pressure-transmitting fluid was used, and the  $PbF_2$  crystal was in direct contact with the fluid. Pressures were determined directly with a calibrated 100,000 psi Heise-Bourdon-Tube gauge.

## EXPERIMENTAL RESULTS

The measured dependence of  $T_1$  and  $T_2$  on temperature for both samples is in qualitative agreement with previously published results (2) and the data are reproduced in Figure 1 and Figure 2. The measurements for the data in Figure 1 were made on crystal A with the magnetic field along the [100] crystallographic axis. The lines through the data points are best eye-ball fits to the data points and their slopes yield activation energies for the relaxation processes of  $(Ea)_{T_1} = 0.205 \pm 0.01$  eV/ion and  $(Ea)_{T_2} = 0.27 \pm 0.01$  eV/ion. The  $T_2$  measurements at a frequency of 56.4 MHz on crystal B yielded

an activation energy of  $0.26 \pm 0.02$  eV/ion. The difference between  $(Ea)_{T_1}$  and  $(Ea)_{T_2}$  is well outside experimental error, and indicates the probability that the relaxation process that is responsible for  $T_1$  is different than that for  $T_2$ . Earlier cruder measurements of activation energies for  $T_2$  in more heavily doped and impure crystals yielded values of 0.32 eV/ion<sup>(2)</sup> and 0.35 eV/ion<sup>(1)</sup>. All these numbers differ greatly from the numerous results near 0.6 - 0.7 eV/ion for the activation energy of  $T_2$  for  $PbF_2$  without the NaF dopant (2,3,7,8).

The results of  $T_{1r}$  measurements on sample A, from  $-50^\circ C$  to  $160^\circ C$  are presented in Figure 3. The measurements were made at 32 MHz with the applied magnetic field along the [100] crystallographic axis, and with rotating fields  $B_1$  of 6.7 G, 14.0 G and 25.8 G. The solid curves that are drawn in are again eye-ball fits to the data; and look approximately like theoretical formulas for  $T_{1r}$  vs.  $1/T$  for motionally narrowed solids<sup>(14)</sup>, where  $T$  is the absolute temperature of the sample. That is, (1) there are well defined  $T_{1r}$  minima in the  $T_{1r}$  vs.  $1/T$  curves, (2) that on the low temperature side of the  $T_{1r}$  minima all three curves are parallel to one another and have an activation energy of  $0.29 \pm 0.02$  eV/ion, and that  $(T_{1r})^{1/2} \propto B_1$  (the best fit occurs for  $B_{loc} \sim 2.8$  G added to  $B_1$ , which was also the case for gypsum<sup>(14)</sup>), (3) that the three curves come together on the high temperature side of the  $T_{1r}$  minimum. Unlike the gypsum case, the slope of the  $T_{1r}$  vs.  $1/T$  curve on the high temperature side of the  $T_{1r}$  minimum is not the negative of the curve on the low temperature side, but has a somewhat smaller slope, and the curves are therefore somewhat

asymmetric.

The activation energy for the  $T_{1r}$  process is within experimental error of that for  $T_2$ , and is consistent with fluorine motion being responsible for  $T_2$  and  $T_{1r}$ . An estimate of the correlation time of this motion can be made from the relation<sup>(14)</sup> that  $2 \gamma B_1 \tau_c \approx 1$  at the  $T_{1r}$  minima, where  $\gamma$  = magnetogyric ratio of fluorine. The  $T_{1r}$  curve for  $B_1 = 25.8$  G has a  $T_{1r}$  minimum value of 0.65 msec at  $T^{-1} = 3.04 \times 10^{-3} \text{ K}^{-1}$  (corresponding to 56°C) and an estimated correlation time of 0.74  $\mu\text{sec}$  using the above relation. The measured  $T_1$  at 56°C is 0.31 sec.

Figure 4 summarizes the results of the pressure-dependent measurements. These were done at 56.4 MHz, at room temperature (292 K) on crystal B. The  $T_1$  decreased monotonically to 430 K (at 56.4 MHz), the highest temperature measured and motional narrowing of  $T_2$  began near 200 K. Thus, at room temperature this sample is well into the motional narrowing region.

As Figure 4 indicates,  $T_2$  decreased by 27% in four kilobars of applied pressure, while  $T_1$  remained within 3% of its initial value. An activation volume for the fluoride ion motion can be obtained from the line placed through the  $T_2$  measurements as a function of pressure. The activation volume,  $V_a$ , is defined by

$$V_a = [\partial G_a / \partial p]_T$$

where  $G_a$  is the Gibb's Free Energy of Activation. Using equations derived by Hultsch and Barnes<sup>(15)</sup> appropriate to a random diffusion model, one relates the activation volume to the pressure dependence of

$T_2$ :

$$V_a = -RT \left[ \frac{\partial \ln(T_2)}{\partial p} + \beta(2 - \gamma_G) \right]_T \quad (1)$$

The second term on the right can be shown to be negligible for  $\text{PbF}_2$  since: (a) the compressibility,  $\beta$ , for  $\text{PbF}_2$  is  $\sim 1.638 \times 10^{-3} \text{Kbar}^{-1}$ , (b) the Grünerisen constant,  $\gamma_G$ , is close to 2, and (c) the value of  $\left(\frac{\partial \ln(T_2)}{\partial p}\right)_T$  is large,  $\sim 7.3 \times 10^{-2} \text{Kbar}^{-1}$ . Thus, we calculate an activation value of  $1.76 \pm 0.05 \text{ cm}^3/\text{g-mole}$  from the  $T_2$  curve. We can also obtain an activation value from the  $T_1$  curve by similar argument<sup>(15)</sup>. It is estimated to be a maximum at  $0.2 \text{ cm}^3/\text{g-mole}$  from the data in Figure 4.

The lack of agreement between  $T_2$  and  $T_1$  results can best be illustrated in another fashion. From the measured temperature dependence of  $T_2$  on this crystal, one predicts it would be necessary to lower the temperature 8 K (to 284 K) to obtain the equivalent 27% decrease in  $T_2$  that was observed as a function of pressure in four kilobars. However, a lowering of the temperature from 292 K to 284 K would have also increased  $T_1$  by 20%, and this qualitatively disagrees with the high pressure results for  $T_1$ . The dotted line in Figure 3 is the predicted behavior of  $T_1$  using this argument, and one observes the lack of agreement with the experimental results. If the motion were controlled by a single parameter model, it would normally be possible to map between the temperature-dependence and the pressure-dependence plots (one ignores quantitative corrections here such as the change in size of the static dipolar interaction due to small interatomic distance changes since they would not affect the conclusions to any significant degree). The implication when such mapping attempts fail is that a single parameter model

is not sufficient to account for the temperature and pressure dependence of both  $T_1$ , and  $T_2$  and  $T_{1r}$ .

We have also measured the  $T_1$  near room temperature of both samples at several other frequencies. All evidence, including  $T_1$  decreasing with increasing temperature indicates the two samples being in the long correlation time region if the  $T_1$  mechanism involves diffusive motion of the fluorine atoms. Then,  $T_1$  should be proportional to  $f_0^{-2}$ , where  $f_0$  is the measuring frequency. We found that the measured  $T_1$  of crystal A at 306 K was the same to within experimental error (10%) at 60 MHz and 32 MHz. A similar measurement on crystal B at 292 K showed  $T_1$  was only 20% smaller at 12.5 MHz than at 56.4 MHz, instead of decreasing by a factor of 20.

#### DISCUSSION AND CONCLUSIONS

The results reported here generally confirm the earlier obtained preliminary results<sup>(2)</sup> for NaF doped  $\beta$ -PbF<sub>2</sub>. However the crystals used for this study had dopant levels an order of magnitude lower, and more parameters were measured. The data show that  $T_1$ ,  $T_2$ ,  $T_{1r}$  are strongly dependent upon the dopant level, and that their corresponding activation energies are different than those of pure  $\beta$ -PbF<sub>2</sub>.

The  $T_1$  of the two doped crystals studied is much shorter than for the pure material, at the same temperature. At a temperature of 292 K, the measured values of the  $T_1$ 's of crystal A (0.02% dopant) and B (0.12% dopant) are 0.7 sec. and 0.1 sec. respectively. The ratio of the doping

levels is  $N_B/N_A \approx 6$ . Any number of different relaxation mechanisms ( motional effects dominating  $T_1$ , etc.) predict  $T_1 \propto \frac{1}{N}$ . Our measured  $T_1$ 's yield  $T_{1A}/T_{1B} = 7$  which is close to the ratio of doping levels and suggests that the dopant is responsible for the spin lattice relaxation process.

At temperatures where motional narrowing is observed, the  $T_2$ 's of the two doped crystals studied are much longer when in the motionally narrowed region than that for the pure material at the same temperature. This again suggests that the dopant dominates the motional narrowing of the fluorine atoms. Again assuming that the amount of motion is proportional to the doping concentration leads to  $T_2 \propto N$ . At a temperature of 292 K (well into the strongly motionally narrowed region) we have measured the  $T_2$ 's of both crystals and find a ratio of  $T_{2B}/T_{2A} \sim 6.5$ . This suggests that the NaF dopant is responsible for the rapid fluorine motion. It should be pointed out here that in order for there to be a significant amount of motional narrowing of the fluorine line shape, all the fluorine have to be moving around, not just those near the Na atoms.

As mentioned in the previous section, a direct measure of the rate of fluorine motion can be obtained from the minimum of the  $T_{1\rho}$  curve, and a correlation time of 0.74  $\mu\text{sec}$  for fluorine motion at  $56^\circ\text{C}$  was derived. An estimate of the fluorine self diffusion coefficient can be made from the formula  $D \sim a^2/6\tau$  where  $a$  is a fluorine jump distance and  $\tau$  is the time between jumps. Using a value of  $a = 2.964 \text{ \AA}$ , the nearest neighbor fluorine-fluorine distance, and setting  $\tau$  equal to our measured correlation time,  $D_A(56^\circ\text{C}) \approx 2.0 \times 10^{-10} \text{ cm}^2/\text{sec}$ . The estimated value

of D for crystal B is 6.5 larger, that is  $D_B(56^\circ\text{C}) = 13 \times 10^{-10} \text{ cm}^2/\text{sec}$ .

The parameters  $T_1$ ,  $T_2$  and  $T_{1r}$  depend directly upon the NaF doping level, as discussed above, but there are enough differences between the behavior of  $T_1$  from  $T_{1r}$  and  $T_2$ , that we believe the relaxation mechanism for  $T_1$  is not that responsible for  $T_2$  and  $T_{1r}$ , that is modulation of the fluorine dipole-dipole interaction by fluorine motion. Evidence for this is

- (1) the difference for the activation energies of  $T_1$  with  $T_2$  and  $T_{1r}$  for crystal A as listed in Table I is well outside experimental error.
- (2)  $T_1$  is essentially pressure independent while  $T_2$  shows a strong pressure dependence.
- (3)  $T_1$  is essentially independent of the applied magnetic field  $B_0$  even though  $\tau_c$  is long enough at the temperature where field dependence was studied, that the sample was definitely in the long correlation time region where  $T_1 \propto B_0^2$ .

A crude estimate of the contribution to  $T_1$  and  $T_{1r}$  due to motional modulation of the fluorine dipole-dipole interaction can be made from Equations 2 and 3 below<sup>(16,17)</sup>.

$$\frac{1}{T_1} \approx \frac{2}{3} \gamma^2 M_2 \left( \frac{1}{\omega_0^2 \tau_c} \right) \quad (\text{long correlation time region}) \quad (2)$$

$$\frac{1}{T_{1r}} \approx \frac{1}{2} \gamma^2 M_2 \left( \frac{\tau_c}{1 + 4\omega_1^2 \tau_c^2} \right) \quad (3)$$

$M_2$  is the unarrowed second moment of the fluorine line,  $\gamma$  is the

magnetogyric ratio of the fluorine nucleus, and  $\omega_0 = \gamma B_0$ ,  $\omega_1 = \gamma B_1$  where  $B_0$  is the strength of the applied magnetic field,  $B_1$  the amplitude of the rotating field. The measured  $M_2$  for  $B_0$  along the [100] crystal axis is  $52.4 \times 10^8 \text{ sec}^{-2}$ . In the previous section, the  $\tau_c$  at  $56^\circ\text{C}$  (from the  $T_{1r}$  minimum) was inferred to be  $0.74 \text{ } \mu\text{sec}$ . for crystal A. Using these values, we estimate  $T_1$  and  $T_{1r}$  and compare them to their measured values in Table II. The ratio of the calculated to measured values of  $T_{1r}$  is 1.6. Considering the crudeness of the calculation, this is good agreement and suggests that motional modulation of fluorine-dipole-dipole interaction is the dominant  $T_{1r}$  mechanism. The same model and crudeness of calculation leads to a ratio of calculated to measured value of  $T_1$  of 27.6. This is more than an order of magnitude worse than the  $T_{1r}$  case and suggests that the NaF dopant produces a more effective  $T_1$  mechanism that does not involve motional modulation of the fluorine dipole-dipole interaction and has a different activation energy for it. In addition, this mechanism is independent of measuring magnetic field (that is, it is in the short correlation time region), and is insensitive to applied hydrostatic pressures.

A  $T_1$  mechanism that fits all these criteria is relaxation via electronic carriers. Undoped  $\text{PbF}_2$  has n-type electronic conductivity which can be enhanced further by doping with trivalent rare earth ions as observed by Arkhangel'skaya et al<sup>(5)</sup> in the temperature range 200-300 K. Doping with monovalent cations enhances the p-type character, with impurities as acceptors. Similar effects have been detected by Wagner et al<sup>(19)</sup> in  $\text{PbCl}_2$ -1% KCl and  $\text{PbBr}_2$ -1% KBr systems in which the p-type electronic conductivity was found to be  $10^{-4}$  of the total, at

573 K.

The contribution to the  $T_1$  due to carriers in the semiconductor is calculated for a model which assumes scalar contact interaction between the carriers and the nuclear spins, and Boltzmann statistics for the carriers in the valence band. The results are

$$\frac{1}{T_1} = \left(\frac{32}{9}\right) \gamma_e^2 \gamma_n^2 N l \eta^2 (2\pi m_1 m_2 m_3 kT)^{1/2} \quad (4)$$

where  $N$  is the carrier density;  $l$  is the number of equivalent maxima in the valence band;  $m_1$ ,  $m_2$  and  $m_3$  are the anisotropic effective mass,  $\eta$  is the carrier density at the nucleus (assumed constant over the Fermi surface)<sup>(18)</sup>.

In the freeze-out range where carrier density is thermally activated, the temperature-dependence of  $1/T_1$  should be dominated by  $e^{-E_a/kT}$  where  $E_a$  is the thermal activation energy. From the plot of  $T_1$  vs.  $1/T$  in Figure 1, we see that the curve is well-behaved and described by an activation energy of  $0.21 \pm 0.01$  eV. This model and number are consistent with  $T_1$  data of the 0.4% NaF-doped polycrystalline  $PbF_2$  sample in the lower temperature region<sup>(2)</sup>. This activation energy of acceptor state is also compatible to that of donor state at 0.38 eV measured by J. Schoonman et al.<sup>(8)</sup>. For temperatures above the freeze-out region, the carrier density saturates to a constant value, determined by the doping level. This is again consistent with the previously reported data<sup>(2)</sup> for both  $T_1$  and  $T_2$  measurement in the high temperature region.

REFERENCE

1. M. Mahajan and B. D. Nageswara Rao, Chem. Phys. Lett. 10,29 (1971).
2. T. Y. Hwang, M. Engelsberg and I. J. Lowe, Chem. Phys. Lett. 30, 303 (1975)
3. J. Schoonman, L. B. Ebert, C-H. Hsieh, and R.A. Huggins, J. Appl. Phys. 46, 2873 (1975)
4. C. E. Derrington and M. O'Keefe, Nature 246,44 (1973).
5. V. A. Arkhangel'skaya, V. G. Erofeichev, and M. N. Kiseleva, Sov. Phys.-Solid State 14, 2953 (1973).
6. A. F. Halff, J. Schoonman, and A. J. H. Eykelenkamp, J. Phys. 34, C9 (1973).
7. J. H. Kennedy, R. Miles, and J. Hunter, J. Electrochem. Soc. 120, 1441 (1973).
8. J. Schoonman, G.J.Dirksen, and G. Blasse, J. Solid State Chem. 7, 245 (1973).
9. A.V. Joshi and C. C. Liang, J. Phys. Chem. Solids 36, 927 (1975).
10. C. C. Liang and A. V. Joshi, J. Electrochem. Soc. 122, 466 (1975).
11. I. J. Lowe and C. E. Tarr, J. Sci. Instr. 1,604 (1968); 1, 320 (1968).
12. R. W. Vaughan, D. D. Elleman, L. M. Stacey, W-K. Rhim, and J.W. Lee, Rev. Sci. Instr. 43, 1356 (1972).
13. G. B. Benedek, Magnetic Resonance at High Pressure. Interscience Publishers, 1963.
14. D. C. Look and I. J. Lowe, J. Chem. Phys. 44, 2995 (1966).
15. R. A. Hultsch and R.G. Barnes, Phys. Rev. 125,6 (1962).
16. D. E. O'Reilly and T. Tsang, Phys. Rev. 157, 417 (1967).
17. D. E. Barnaal, M. Kopp and I. J. Lowe, J. Chem. Phys. (to be published)
18. A. Abragam, The Principles of Nuclear Magnetism, Oxford University Press, 1961, page 390.
19. J. B. Wagner and C. Wagner, J. Electrochem. Soc. 104, 509 (1957).

TABLE I

## Summary of Relaxation Time Parameters

Parameter	Activation Energy ev/ion	Crystal	Reference	Comments
$T_1$	$0.205 \pm 0.01$	A	a	$f_o = 32$ and $60$ MHz $B_o$ along [100]
$T_1$	---	B	a	$V_a < 0.2 \text{ cm}^3/\text{g-mole}$ Independent of frequency from $12.5$ MHz to $56.4$ MHz
$T_{1r}$	$0.29 \pm 0.02$	A	a	$f_o = 32$ MHz, $B_o$ along [100] $B_1 = 25.8$ G, $\tau_c \approx 0.74 \mu\text{sec}$ at $56^\circ\text{C}$
$T_2$	$0.27 \pm 0.01$	A	a	$f_o = 32$ MHz $B_o$ along [100]
$T_2$	$0.26 \pm 0.02$	B	a	$f_o = 56.4$ MHz $V_a = 1.76 \pm 0.05 \text{ cm}^3/\text{g-mole}$
$T_2$	$0.32$	$0.4\% \text{ N F}$ polycrystalline	2	$f_o = 32$ MHz
$T_2$	$0.73$	pure	2	$f_o = 32$ MHz
$T_2$	$0.35$	impure polycrystalline	1	$f_o = 8$ MHz C. W. measurement

a = This work

 $V_a$  = Activation Volume

TABLE II

Measured and Calculated Values for  $T_1$  and  $T_{1r}$  for Crystal A at 56°C

---

	Measured	Calculated	Ratio ( $\frac{\text{calculated}}{\text{measured}}$ )
$T_1$ ( sec. )	0.31	8.56	27.6
$T_{1r}$ (msec.)	0.65	1.03	1.6

FIGURE CAPTIONS

- Fig. 1. Log of the  $^{19}\text{F}$  spin-spin relaxation rate ( $T_2$ ) and spin lattice relaxation rate ( $T_1$ ) as a function of inverse temperature for crystal A. Measuring frequency is 32 MHz with magnetic field along [100] crystal axis.
- Fig. 2. Log of the inverse  $^{19}\text{F}$  spin-spin relaxation rate ( $T_2^{-1}$ ) and spin lattice relaxation rate ( $T_1^{-1}$ ) as a function of inverse temperature for crystal B. Measuring frequency is 56.4 MHz.
- Fig. 3. Log of the  $^{19}\text{F}$  spin-spin relaxation rate in the rotating frame ( $T_{1r}$ ) as a function of inverse temperature for crystal A. The measuring frequency is 32 MHz with magnetic field along 100 crystal axis. Rotating magnetic fields are 25.8 G, 14.0 G and 6.7 G.
- Fig. 4. The pressure dependence of the spin-spin ( $T_2$ ) and spin-lattice relaxation times as a function of pressure to 4 kilobars for crystal B at 292 K. The solid line placed through the  $T_2$  data furnishes an activation volume for motion of  $1.76 \pm 0.05 \text{ cm}^3/\text{g-mole}$ . The dotted line is the predicted  $T_1$  behavior given the temperature dependence of  $T_1$  and  $T_2$  and the pressure dependence of  $T_2$ , and assuming a single parameter model of the motion.

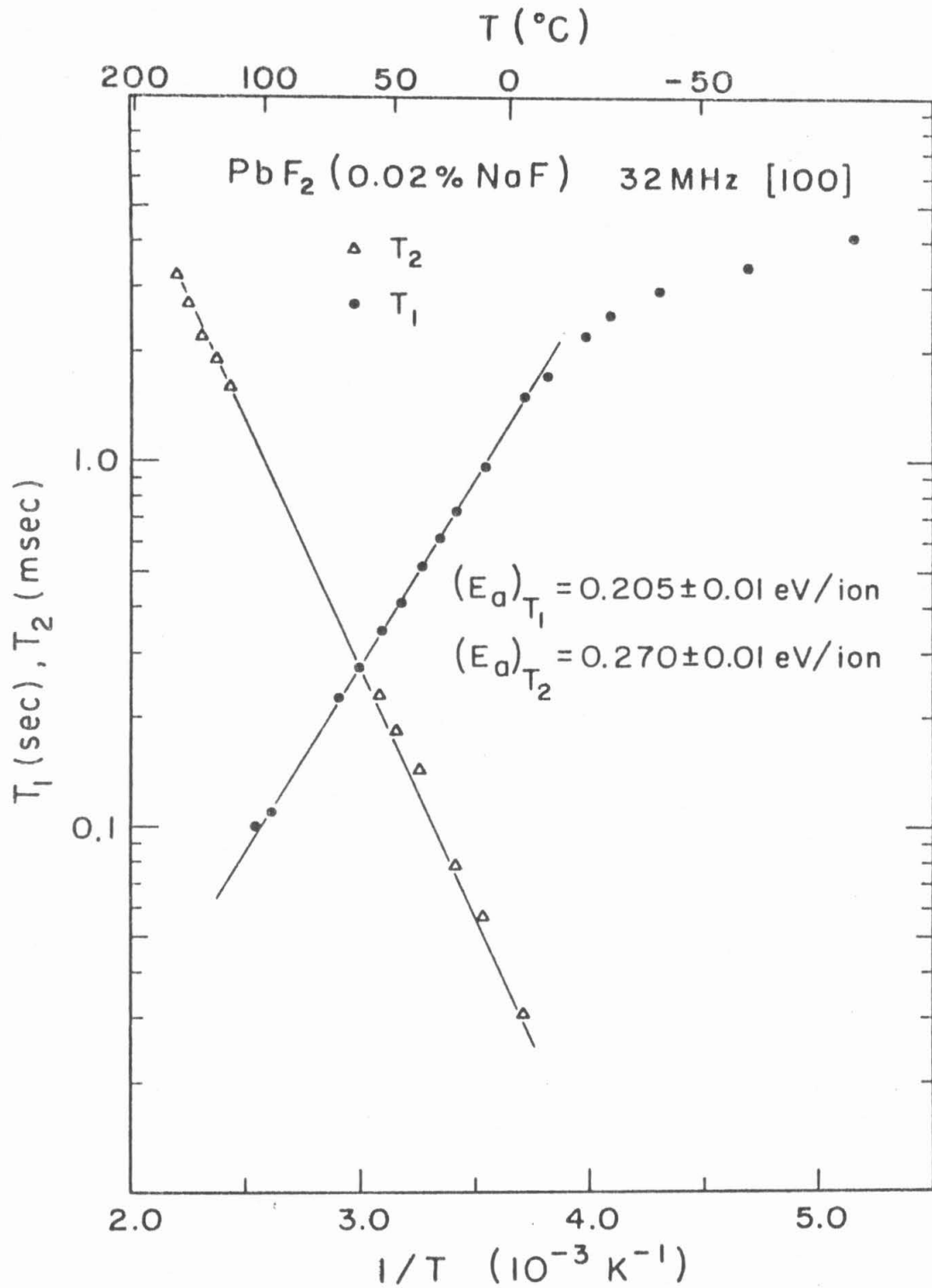
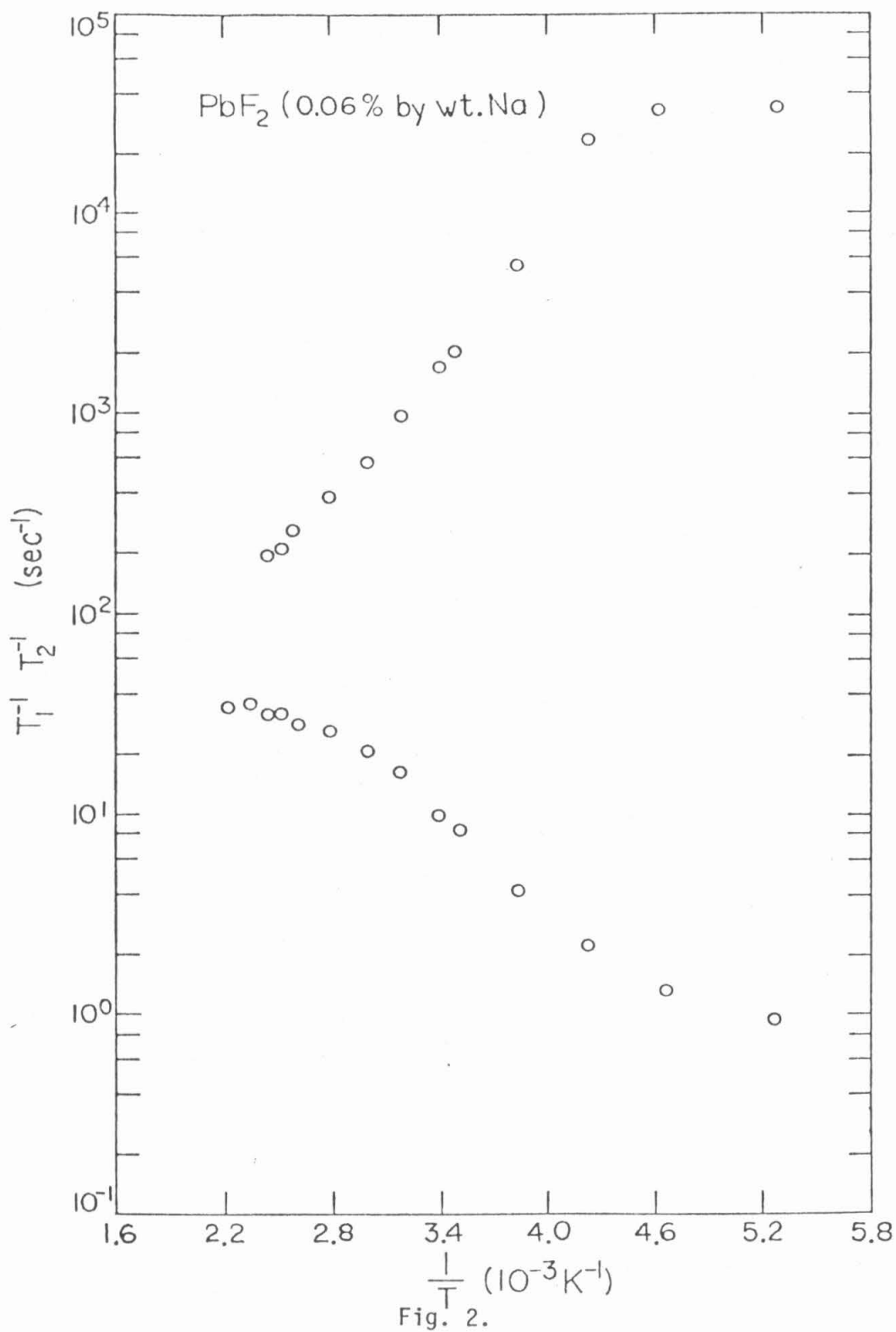


Fig. 1.



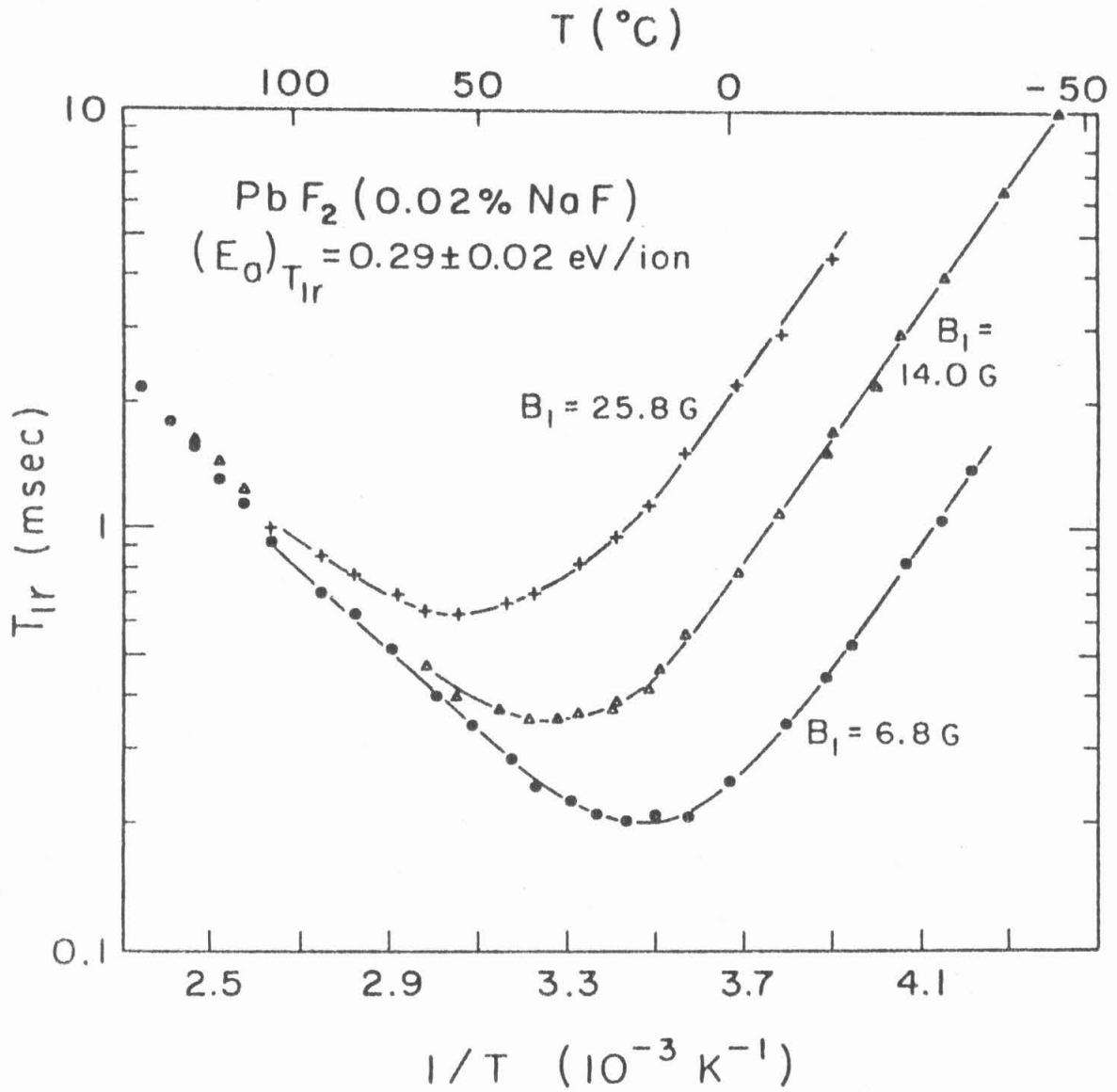


Fig. 3.

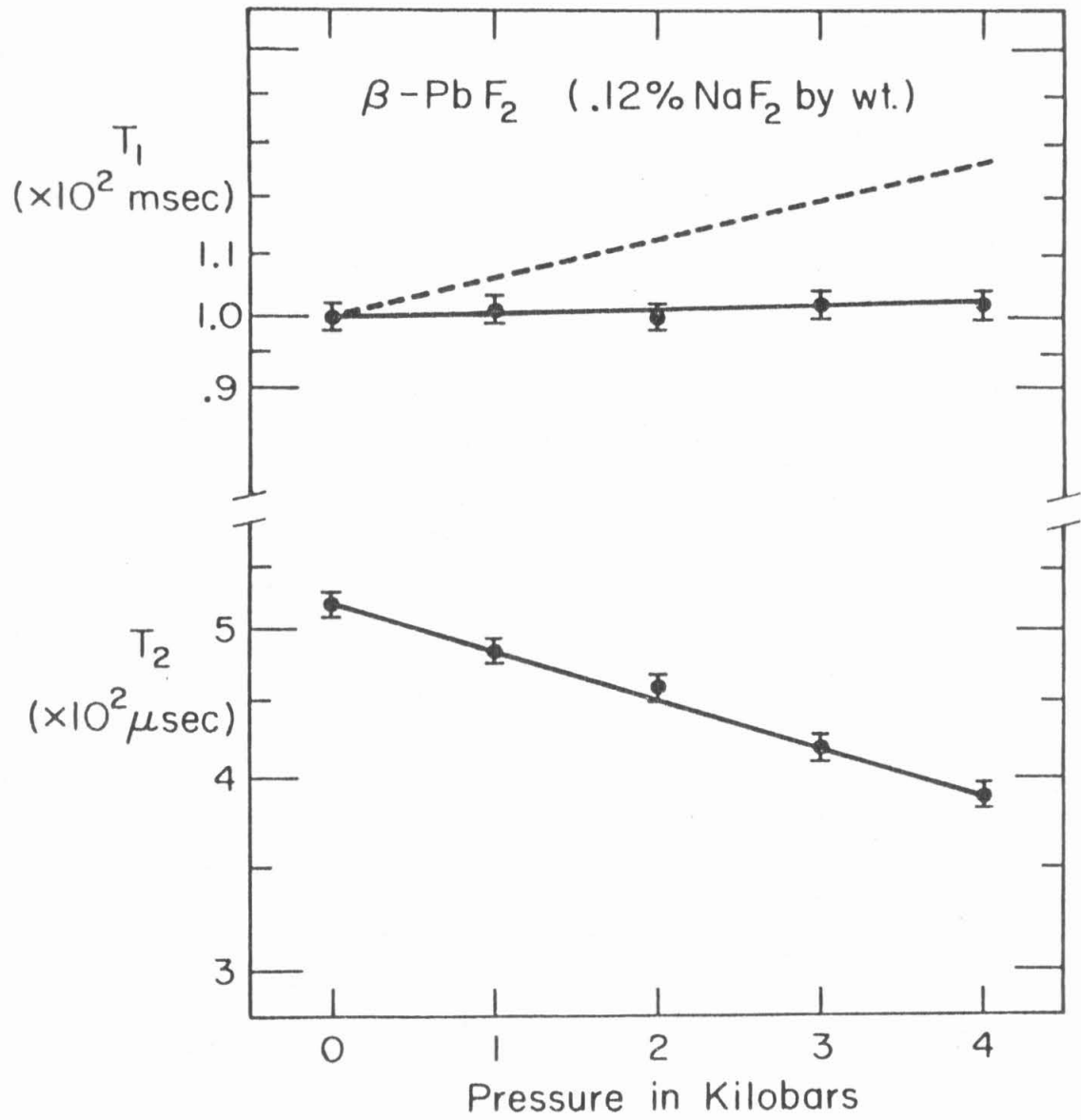


Fig. 4.

CHAPTER 4  
NMR STUDY OF  $\text{Th}_4\text{H}_{15}$

## INTRODUCTION

The problem of understanding the state of hydrogen in metals and metal hydrides is a topic of many recent theoretical and experimental investigations<sup>(1)</sup>. It is noted that better understanding of this problem may be able to shed light on a wide range of problems with practical applications, such as hydrogen embrittlement of metals, heterogeneous catalysis, nuclear reactor component design and construction and many others<sup>(2)</sup>. Among the metal hydrides, thorium hydride receives considerable interest because the higher hydride,  $\text{Th}_4\text{H}_{15}$ , has been experimentally shown to be a superconductor at low temperature (below  $\sim 8.2$  K)<sup>(3)</sup>. Only one other hydride,  $\text{PdH}_x$ , exhibits similar properties<sup>(4)</sup>. It is also interesting to note the hydrogen concentration in  $\text{Th}_4\text{H}_{15}$ : the hydrogen density of  $\text{Th}_4\text{H}_{15}$  ( $0.079 \text{ atom}/\text{\AA}^3$ ) is higher than that of solid hydrogen ( $0.044 \text{ atom}/\text{\AA}^3$ ) and even that of water ( $0.066 \text{ atom}/\text{\AA}^3$ ).

Previous NMR studies on  $\text{Th}_4\text{H}_{15}$  have included: a wideline experiment to measure chemical shift as well as activation energy,  $\Delta E$ , of proton motion from linewidth data<sup>(5)</sup>; a pulse experiment to obtain  $\Delta E$  from  $T_1$ ,  $T_2$  data<sup>(6)</sup>; and  $T_1$  measurements at low temperatures to obtain information on the conduction electron properties<sup>(7)</sup>. All studies used powder samples, and the first wideline work used a sample identified as  $\text{ThH}_{3.5}$ , not felt to be exactly the same composition as the samples in the latter two experiments. In the present work two samples carefully prepared to within 1% of the stoichiometric composition  $\text{ThH}_{3.75}$  were studied using a combination of pulse techniques. The lineshape was obtained from the on-

resonance free induction decay signal; the relaxation times  $T_1$ ,  $T_2$ , and  $T_{1r}$  were measured as a function of temperature; and the dependence of line shift on temperature was measured using the eight-pulse line narrowing technique. Information on the motional and electronic properties is presented from this more complete NMR study. The results are different from those obtained in previous work<sup>(5,6,7)</sup> and indicate that considerable care is needed in the preparation and characterization of the sample.

#### EXPERIMENTAL DETAILS

The two samples of  $\text{Th}_4\text{H}_{15}$  in this study, identified as HP and LP samples, were both in the form of black powders and were prepared by Professor Satterthwaite and his group at the University of Illinois such that the hydrogen-to-thorium ratio was  $3.75 \pm 0.01$ . They were sealed in glass tubes with a partial pressure of helium. The HP sample was prepared under high pressure and high temperature conditions, while the LP sample was prepared under atmospheric pressure.

The pulse spectrometer operates at 56.4 MHz and has been described elsewhere<sup>(8)</sup>.  $T_1$  was measured to within  $\pm 4\%$  accuracy by a  $180^\circ$ -t- $90^\circ$  pulse sequence. Lineshapes (i.e.,  $T_2$  at motion-narrowed region) were measured by the free induction decay (FID) signals following a  $90^\circ$  pulse. The  $90^\circ$  pulse width was approximately 2  $\mu\text{sec}$ , and the dead time (the time from the middle of the pulse to the first point of the observable signal) was between 2.5 and 3.0  $\mu\text{sec}$ . A Carl-Purcell cycle was performed from time to time to check the  $T_2$  obtained by the above method and showed no significant difference indicating that no significant inhomogeneous broadening contributes to all the  $T_2$ 's measured.  $T_{1r}$  was measured by a

$90^\circ$  x-pulse followed by an attenuated y-pulse. The length of the y-pulse was varied from 10  $\mu$ sec to 40 msec.

The line-narrowing experiment was performed using the eight-pulse cycle<sup>(9)</sup>. For most experiments the cycle time was set at 42  $\mu$ sec although in some measurements where cycle-time-dependent properties were studied, a 30  $\mu$ sec cycle time has been achieved. In addition to the regular eight-pulse cycle, two more experiments, the "phase pull parallel" and the "phase pull perpendicular" experiments, were performed. The phase-pull perpendicular<sup>(10,11)</sup> experiment is a modification of the eight-pulse cycle performed by deliberately creating a phase error in one of the x-pulse channels; the magnetization is prepared to point perpendicular to the phase-error averaged Hamiltonian before the pulse cycles operate. The phase-pull parallel experiment is a similar modification except that the magnetization is prepared parallel with the phase-error averaged Hamiltonian. The regular eight-pulse cycle eliminates most of the homonuclear dipolar interaction while the phase-pull perpendicular experiment eliminates, in addition, the chemical shift Hamiltonian. The phase-pull parallel experiment, on the other hand, is similar to a  $T_{1\rho}$  experiment in which the residual dipolar interaction as well as the chemical shift are eliminated.

The temperature range of 40 to 460 K was achieved by two probes with different constructions. The probe with a temperature range of 190 to 460 K used nitrogen gas as the coolant. The low-temperature probe, connected through a liquid helium transfer line<sup>(12)</sup> to a liquid helium dewar, used helium as coolant.

Chemical shifts were measured with the eight-pulse cycle. Between

180 K and room temperature the reference was acetylene chloride. The shift of this reference was measured from the FID signal relative to a TMS reference at room temperature. At a given temperature the shift of the sample was measured with respect to the reference, and the scaling factor of the eight-pulse cycle was determined for that temperature, thus calibrating out any temperature-induced effect due to electronics<sup>(10)</sup>. At lower temperatures the reference was a single crystal of  $\text{Ca}(\text{OH})_2$  oriented in the magnetic field such that the major axis of its proton chemical shift tensor was parallel to the external field. It is assumed that the proton chemical shift of the  $\text{Ca}(\text{OH})_2$  remains unchanged as the temperature is varied. This statement was checked, to a certain extent, by measuring its shift relative to a gypsum powder sample. The error limit of the reported line shift was set liberally at  $\pm 5$  ppm because magnetic susceptibility and electron conductivity of the sample could affect the resonance position in the eight-pulse measurement, and the sample occupied volume in which the external reference indicated that some effective field gradients existed.

## RESULTS AND DISCUSSION

### A. Rigid Lattice Lineshape

As temperature was lowered from room temperature to about 40 K, the FID lineshape of both  $\text{Th}_4\text{H}_{15}$  samples (HP and LP) remained unchanged. No difference was noticed between the two lineshapes. This indicates that no additional "freezing out" of the motion has occurred, and at room temperature the motion of protons in both samples is not sufficiently rapid for motional line narrowing to occur. The on-resonance free

induction decay signal (Figure 1) shows a beat structure, which would not occur if the resonance line were Gaussian. To see if this lineshape is indeed consistent with the structure of  $\text{Th}_4\text{H}_{15}$  reported in the literature<sup>(13,14)</sup>, the second and fourth moments of the experimental lineshape were determined by fitting the experimental FID curve with a polynomial of the form:

$$Q(t) = 1 - \frac{M_2}{2!} t^2 + \frac{M_4}{4!} t^4 - \frac{M_6}{6!} t^6 + \frac{M_8}{8!} t^8 \dots$$

The result of the fit leads to a second moment,  $(M_2)^{1/2}$ , of  $4.42 \pm 0.13$  Gauss and a fourth moment,  $(M_4)^{1/4}$  of  $5.39 \pm 0.21$  Gauss. The procedure for obtaining these numbers requires some elaboration at this point:

the moments obtained from least square fit of this type depend on the dead time, the number of data points, and the order of polynomial fitted. By changing all these variables one can determine the sensitivity of the results to these variables and their values. In general, higher moments become important only at long times, and for lower moments lower order polynomials are sufficient. The above numbers quoted for the second and fourth moments were obtained from averaging many of the "reasonable values" from various fits up to  $t^8$  term in  $Q(t)$ , with dead time of either 2.5  $\mu\text{sec}$  or 3.0  $\mu\text{sec}$ . The error limit covers the range of these "reasonable values." These errors are small because of the large signal-to-noise ratio of the experimental data and the short dead time of the spectrometer.

Using the reported structure of the sample, theoretical second and fourth moments were calculated by the following equations appropriate for spin 1/2 nuclei in a powder sample:

$$M_2 = \frac{9}{20} \gamma^4 \hbar^2 \frac{1}{n} \sum_{n,k} \frac{1}{r_{nk}^6} \quad (1)$$

$$\begin{aligned}
 M_4 = & \frac{\gamma^4 \hbar^4}{n} \frac{27}{560} \left\{ 9 \sum_{n,k,l} \left( \frac{1}{r_{nk}} \right)^{12} + \frac{23}{4} \sum_{n,k,l} \frac{1}{r_{nk}^6 r_{nl}^6} \right. \\
 & (2 - \cos^2 \phi_{knl} + \cos^4 \phi_{knl}) \\
 & - \frac{1}{2} \sum_{n,k,l} \frac{1}{r_{nk}^6 r_{kl}^6} (2 - \cos^2 \phi_{nkl} + 3 \cos^4 \phi_{nkl}) \\
 & + 4 \sum_{n,k,l} \frac{1}{r_{nk}^6 r_{nl}^3 r_{kl}^3} \\
 & (\cos^2 \phi_{kln} - \cos^2 \phi_{knl} - \cos^2 \phi_{nkl} + 3 \cos^2 \phi_{knl} \cos^2 \phi_{nkl}) \\
 & - \sum_{n,k,l} \frac{1}{r_{kl}^6 r_{nk}^3 r_{nl}^3} (\cos^2 \phi_{knl} - \cos^2 \phi_{nlk} - \cos^2 \phi_{nkl} \\
 & \left. + 3 \cos^2 \phi_{nlk} \cos^2 \phi_{nkl} \right) \quad (2)
 \end{aligned}$$

n,k,l's are indices for spins

n = 1 if all locations are equivalent

Equation 2 for the fourth moment can be derived from Van Vleck's formula<sup>(15)</sup> by properly averaging over all solid angles. The calculation leads to a second moment,  $(M_2)^{1/2}$ , of 4.48 Gauss and a fourth moment,  $(M_4)^{1/4}$ , of 5.47 Gauss. In the calculation of the second moment all protons within a radius of 12.5 Å were involved, while only 60 protons were involved in the calculation of the fourth moment. The agreement between the theoretical and experimentally determined moments furnishes confirmation of the structure assumed in the theoretical calculation. The non-Gaussian line-

shape is indicated by the ratio  $(M_4)^{1/4}/(M_2)^{1/2}$ . For a Gaussian line this ratio is 1.32 but for  $\text{Th}_4\text{H}_{15}$  it is only 1.22, suggesting a broader line than a Gaussian. The FID signal can be fit well by another type of function in the form of:

$$\exp(-a^2 t^2/2) \sin(bt)/bt \quad \text{where} \quad M_2 = a^2 + \frac{1}{3} b^2; \quad M_4 = 3 a^4 + 2 a^2 b^2 + \frac{1}{5} b^4,$$

as shown in Figure 1. This type of function has also been shown to fit the FID signal of  $\text{CaF}_2$  single crystal quite well<sup>(16)</sup>.

### B. Relaxation Times and Motional Properties

In a simple description the motion of nuclei in solids can be described by a correlation time  $\tau$  which obeys the equation

$$\frac{1}{\tau} = \frac{1}{\tau_0} e^{-\Delta E/kT}$$

where  $\Delta E$  is the activation energy of the motion of nuclei carrying the spins. More specifically,  $\tau$  can be interpreted roughly as the averaged time in between jumps of a nucleus. To extract  $\Delta E$  and  $\tau$  from NMR measurements, one can use the following approximate equations appropriate for relaxation times controlled by modulation of dipolar interaction due to motion of nuclear spins<sup>(17,18)</sup>:

$$\frac{1}{T_2} \approx \gamma^2 M_2 \tau \quad \text{in the motional narrowing region} \quad (3)$$

$$\frac{1}{T_1} \approx \frac{2}{3} \gamma^2 M_2 \left( \frac{1}{\omega_0^2 \tau} \right) \quad \omega_0 \tau \gg 1 \quad (4)$$

$$\frac{1}{T_{1r}} \approx \frac{1}{2} \gamma^2 M^2 \left( \frac{\tau}{1 + 4\omega_1^2 \tau^2} \right) \quad (5)$$

$\omega_0$ : Larmor frequency corresponding to external  $H_0$  field.

$\omega_1$ : Larmor frequency corresponding to rf  $H_1$  field.

and from Equations 3 to 6, one obtains:

$$\begin{aligned} \Delta E &= R \left[ \frac{\partial \ln\left(\frac{1}{T_2}\right)}{\partial\left(\frac{1}{T}\right)} \right]_p \\ \Delta E &= -R \left[ \frac{\partial \ln\left(\frac{1}{T_1}\right)}{\partial\left(\frac{1}{T}\right)} \right]_p \\ \text{or } \Delta E &= -R \left[ \frac{\partial \ln\left(\frac{1}{T_{1r}}\right)}{\partial\left(\frac{1}{T}\right)} \right]_p \quad \omega_1 \tau \gg 1 \end{aligned} \quad (6)$$

Thus,  $\tau$  can be estimated by several different measurements and  $\Delta E$  is obtained by fitting the slope of a plot of  $\ln\left(\frac{1}{T_2}\right)$ ,  $\ln\left(\frac{1}{T_1}\right)$ , or  $\ln\left(\frac{1}{T_{1r}}\right)$  as a function of  $1/T$  ( $T$  is the temperature in K).

Other measurements such as the eight pulse, eight-pulse phase-pull parallel, and eight-pulse phase-pull perpendicular experiments were all observed to be dependent on temperature (see Figure 2). Theory of motion on these effects has not been well established, and at this stage these measurements have not been interpreted to furnish motional information.

Since major differences in the motional properties of protons were found between the HP and LP samples, their results will be discussed separately.

### Motional Data of the LP Sample

The motional data of the LP sample are summarized in Figure 3. Line shape measurements indicate that motional narrowing starts at around 60<sup>0</sup> C, although this is not shown in the figure because the 1/e decay time has not been changed much at this temperature. By 110<sup>0</sup> C, the lines appear completely Lorentzian. Activation energy obtained from T<sub>2</sub> above 120<sup>0</sup> C is 16.3 ± 1.2 kcal/mole.

The observed T<sub>1</sub> consists of two contributions:  $1/T_1 = 1/T_{1e} + 1/T_{1d}$ . T<sub>1e</sub> is due to relaxation effect caused by conduction electrons, and T<sub>1d</sub> is due to dipolar relaxation effect caused by the motion of nuclear spins. At temperatures below 110<sup>0</sup> C, the conduction electron effect completely dominates the T<sub>1</sub>, and when T<sub>1</sub> is plotted against  $\frac{1}{T}$  as in Figure 4, the T<sub>1</sub> curve can be fitted by a straight line through the origin. The product T<sub>1</sub>T is 180 ± 10 K-sec. This is different from the value of 120 K-sec obtained in the previous work<sup>(7)</sup>. At higher temperatures the relaxation due to the proton motion begins to dominate. By subtracting out the conduction electron contribution, one obtains an activation energy of 18.0 ± 3.0 kcal/mole from the T<sub>1d</sub> contribution, in good agreement with the activation energy from the T<sub>2</sub> data.

T<sub>1r</sub> data indicate that T<sub>1r</sub> is proportional to H<sub>1</sub><sup>2</sup>, the square of the rf field strength. This strongly suggests that T<sub>1r</sub> is dominated by motional effect. The two sets of T<sub>1r</sub> curves in Figure 3 appear straight and seem to lie in the ω<sub>1</sub>τ >> 1 region. The activation energy of proton motion below 80<sup>0</sup> C obtained is 10.9 ± 0.7 kcal/mole. The difference between the activation energies (16.3 ± 1.2 or 18.0 ± 3.0 kcal/mole

above  $120^{\circ}$  C and  $10.9 \pm 0.7$  kcal/mole below  $80^{\circ}$  C) is outside the limit of experimental error and suggests several mechanisms for the proton motion.

In addition to activation energies, Equations 3, 4, and 5 can be used to obtain the correlation time  $\tau$  of the proton motion. It turns out that  $\tau$ 's derived from  $T_2$  data are approximately five times the  $\tau$ 's from the  $T_1$  data. The discrepancy can be attributed to the crude nature of the theory used and may indicate that correlative motion exists which invalidates the use of equations derived from a single correlation time formulation. Experimental determination of the  $T_1$  min's corresponding to  $H_1 = 4.7$  G and  $H_1 = 20.6$  G was not possible. If one uses the approximate expression of Equation 5, one obtains for  $H_1 = 4.7$  G the value of  $1/T_1 \text{ min} = 1.4 \times 10^4 \text{ sec}^{-1}$  and  $\tau = 3.9 \times 10^{-6}$  sec at  $T_1 \text{ min}$ . For  $H_1 = 20.6$  G the values obtained are  $1/T_1 \text{ min} = 3.19 \times 10^3 \text{ sec}^{-1}$  and  $\tau = 8.9 \times 10^{-7}$  sec at  $T_1 \text{ min}$ . An extrapolation of the  $\tau$  curve from  $T_1$  data at temperatures above  $120^{\circ}$  C (using Equation 4) to lower temperatures leads to a  $T_{1r \text{ min}}$  of  $H_1 = 4.7$  G at  $87^{\circ}$  C. For  $H_1 = 20.6$  G the temperature for the  $T_{1r \text{ min}}$  is  $114^{\circ}$  C. These values of  $T_{1r \text{ min}}$  appear reasonable considering the available  $T_{1r}$  data at lower temperatures. Thus, one concludes that the  $\tau$ 's predicted for the temperature range between  $120^{\circ}$  C and  $80^{\circ}$  C from extrapolation of data at higher and lower temperatures agree with one another to within an order of magnitude.

#### Time-Temperature Hysteresis Effect of the HP Sample

Not much difference was found between two samples as the temperature was raised, although the  $T_1$  of the HP sample is slightly shorter than

that of the LP sample (by 10%). Upon cooling, a major difference was found. While data of the LP sample showed no time-temperature hysteresis, a distinctive effect was observed in the HP sample (see Figure 5). A more dramatic manifestation of this is that after the sample was cooled to room temperature, the proton motion took weeks to return to the original state, as indicated by the  $T_2$  and  $T_{1r}$  data (see Figure 6). After the phenomena was observed the first time, the experiment was repeated a month later and the same effect was observed in  $T_1$ ,  $T_2$ , and  $T_{1r}$  measurements.

$T_1$  is dominated at room temperature by conduction electron effects while  $T_2$  and  $T_{1r}$  are controlled by motional properties of the protons. The large time-temperature hysteresis observed in all of these parameters is strongly indicative of a major phase change in the material on heating. The hysteresis is sufficiently large to be difficult to understand without the necessity of moving the thorium atoms to new locations since the mobility of the protons is such that they would relocate in times short compared to these, and the  $T_1$  results are indicative that a change in band structure is associated with the hysteresis. The fact that samples of the same composition and physical characteristics can behave so differently under mild heating is indicative that much still must be learned about this complex material, and it is our understanding that detailed x-ray studies as a function of sample preparation and temperature are being conducted by Professor C. B. Satterthwaite's research group at this time.

#### Summary of the Relaxation Measurements

Questions concerning the detailed mechanism of the motion in  $\text{Th}_4\text{H}_{15}$ ,

such as the question of whether vacancy or the interstitial diffusion mechanism is dominant, cannot be answered by NMR measurements alone. It is clear that proton tunneling does not seem to be an important mechanism due to the large activation energy of motion observed. The existence of several proton motion mechanisms is indicated by the change of activation energy, and correlation motion is suggested by the discrepancy between the  $\tau$ 's predicted by  $T_1$  and  $T_2$  data through Equations 3 and 4. The motional properties reported here differ significantly from previous measurements: the activation energy obtained for a temperature above  $120^{\circ}$  C is two to three times the values obtained in reference (6); motion narrowing of the lineshape occurs at much higher temperature than that in reference (5); and no temperature hysteresis effects have been previously reported. These discrepancies suggest that sample characterization other than composition may be critical to its motional property. The conduction electron effect from this work also differs from the previous result. The product  $T_1T$  in this work is  $180 \pm 10$  K-sec, whereas it was determined to be 120 K-sec by others<sup>(7)</sup>.

### C. Multiple Pulse Measurements and Knight Shift

Just as expected for systems where only one kind of spin is present, the eight-pulse cycle narrowed the lines of both HP and LP samples by  $\sim 30$  times. No significant difference was found between the two samples at  $20^{\circ}$  C and  $-80^{\circ}$  C. Further measurements were thus made only on the LP sample. The eight-pulse line width is due primarily to residual dipolar interactions. This is indicated by the cycle time dependence of the eight-pulse resolution and supported by the small difference between the

decay times of phase alternate (phase-pull perpendicular) and the eight-pulse cycle. The low temperature ( $0^{\circ}$  C and lower) eight-pulse width is wider than that at room temperature, suggesting that some field inhomogeneity type Hamiltonian is present in the sample but is averaged by motion ( $\tau \approx 10^{-4}$  sec) at room temperature. The field inhomogeneity-type Hamiltonian is estimated to be less than 800 Hz by the above-mentioned increase of eight-pulse width and the phase alternate experiment. This means that combination of  $H_0$  inhomogeneity, indirect spin-spin coupling, susceptibility effect due to small particle size, chemical shift or Knight shift anisotropies do not add up to more than this value.

There is evidence that eight-pulse line width is wider after the sample is heated to high temperatures. Some structure was observed in the eight-pulse lineshape at low temperatures before the high temperature experiment. One spectrum at  $\sim 40$  K looked like a powder pattern which may be interpreted as either two proton lines associated with the two types of inequivalent protons in the  $\text{Th}_4\text{H}_{15}$  sample or the combined effect of their chemical shift (or Knight shift) anisotropies. The two peaks were estimated to be separated by 16 ppm, and if it were a single chemical shift tensor with axial symmetry, the chemical shift tensor would be inverted, i.e.,  $\sigma_{\perp} > \sigma_{\parallel}$  other than the usual  $\sigma_{\parallel} > \sigma_{\perp}$  found in most of the hydrogen-bonded solids<sup>(19)</sup>.

After the high temperature experiments, however, the line remained quite wide ( $\sim 2200$  Hz) and symmetrical down to 46 K. Since it may take weeks for the sample to return to its original state and the samples in this work were soon lost, the one spectrum which showed structure cannot be confirmed until further samples are acquired. Line shift data

were taken three days after the sample was heated. The observed shift was corrected for bulk susceptibility effects by assuming both the sample and the reference to be long cylinders. The following equation was used:

$$\delta = \delta_{\text{obs}} + \frac{2\pi}{3} (\chi_{\text{V ref}} - \chi_{\text{V}})$$

$\chi_{\text{V}}$  is the volume magnetic susceptibility. For  $\text{Ca}(\text{OH})_2$ ,  $\chi_{\text{V}} = -0.665 \times 10^{-6}$  and its chemical shift tensor has been measured<sup>(20)</sup>. For  $\text{Th}_4\text{H}_{15}$ , the susceptibility was measured<sup>(22)</sup> to be paramagnetic and dependent on temperature ( $\chi_{\text{V}} \approx +0.93 \times 10^{-6}$  at 12 K and  $+0.57 \times 10^{-6}$  at 273 K, with the assumption that the density of the powder sample is  $4.14 \text{ gm/cm}^3$ , which is half the formula density of  $\text{Th}_4\text{H}_{15}$ ). The corrected shift is thus presented in Figures 7 and 8.

Interpretation of the shift is complicated by the fact that there may be contributions from several interactions including the chemical shift (orbital motion of electrons) and Knight shift (spin magnetic moment or electrons). The absolute chemical shifts of protons in diamagnetic solids are typically of the order near 30 ppm<sup>(19)</sup>, and the Knight shift due to conduction electrons through the contact interaction is estimated to be -31.2 ppm, using the experimental  $T_1T$  value of 180 K-sec and the Korringa relation<sup>(21)</sup>:

$$T_1 \frac{\Delta H}{H} = \frac{\hbar}{\pi kT} \frac{\gamma_e^2}{\gamma_n^2}$$

Both of these contributions are temperature independent, and it seems that some other interaction is responsible for the temperature-dependent shift observed experimentally. Temperature-dependent shifts have been found in several A-15 compounds (e.g.,  $^{51}\text{V}$  and  $^{69,71}\text{Ga}$  in  $\text{V}_3\text{Ga}$ <sup>(23)</sup>) and

are thought to be due to core polarization from d band electrons. Such interaction is not possible for protons, and there is yet no satisfactory explanation for such a shift.

Finally, it should be mentioned that the shift measured in this work is in the opposite direction to that measured in reference (5). Using  $T_1T = 180$  K-sec, one calculates a ratio of:

$$\xi = \frac{\langle \psi(0) \rangle_{Ef}}{\langle \psi(0) \rangle_{atom}}$$

so that

$$0.1 \leq \xi \leq 0.5$$

which is somewhat smaller than the result reported in reference (7), but confirms the fact that a significant portion of the electrons on the hydrogen atom is in the conduction band.

REFERENCES

1. W. M. Mueller, J. P. Blackledge, and G. G. Libowitz, Metal Hydrides (Academic Press, New York, 1968).
2. Ibid. Chapter one.
3. C. B. Satterthwaite and I. J. Toepke, Phys. Rev. Lett. 25, 741 (1970).
4. T. Skoskiewicz, Phys. Stat. Solid 11a, K123 (1972).
5. W. Spalthoff, Z. Fuer Phys. Chem. Neue Folge 29, 258 (1961).
6. J. D. Will and R. G. Barnes, J. Less Common Metals 13, 131 (1967).
7. D. S. Schreiber, Solid State Comm. 14, 177 (1974).
8. R. W. Vaughan, D. D. Elleman, L. M. Stacey, W.-K. Rhim and J. W. Lee, Rev. Sci. Instrum. 43, 1356 (1973).
9. W.-K. Rhim, D. D. Elleman, and R. W. Vaughan, J. Chem. Phys. 58, 1772 (1973); 59, 3740 (1974).
10. W.-K. Rhim, D. D. Elleman, L. B. Schreiber, and R. W. Vaughan, J. Chem. Phys. 60, 4595 (1974).
11. C. R. Dybowski and R. W. Vaughan, Macromolecules 8, 50 (1975).
12. For detailed description of the liquid transfer Heli-Tran refrigerator, see operating manual (Air Product and Chemicals, Inc., Allentown, Pennsylvania).
13. W. H. Zachariasen, Acta Cryst. 6, 363 (1953).
14. J. M. Carpenter, et al., private communication.
15. J. H. Van Vleck, Phys. Rev. 74, 1168 (1948).
16. A. Abragam, The Principle of Nuclear Magnetic Resonance. (Oxford University Press, 1961). Chapter three.
17. N. Bloembergen, E. M. Purcell, and R. V. Pound, Phys. Rev. 73, 679 (1948).

18. D. E. Barnaal, M. Kopp, and I. J. Lowe, J. Chem. Phys. (to be published).
19. K. F. Lau and R. W. Vaughan, Chem. Phys. Letters 33, 550 (1975).
20. L. B. Schreiber and R. W. Vaughan, Chem. Phys. Lett. 28, 586 (1974).
21. J. Koringa, Physica 16, 601 (1950).
22. Private communication, C. B. Satterthwaite and T. Brun.
23. M. Weger and I. B. Goldberg, Solid State Phys. Advances in Research and Application, Vol, 28 (1973).
24. A. M. Clogston and V. Jaccarino, Phys. Rev. 121, 1357 (1961).

FIGURE CAPTIONS

- Fig. 1. Normalized free induction decay signal of the  $\text{Th}_4\text{H}_{15}$  powder sample. The solid line is the empirical fit using a function of the form  $\exp(-a^2t^2/2)\sin(bt)/bt$  together with the calculated second and fourth moments.
- Fig. 2. Log of the inverse of the 1/e decay points of the signal envelopes of the eight pulse and the eight pulse phase pull parallel experiments as a function of inverse temperature for the  $\text{Th}_4\text{H}_{15}$  powder sample.
- Fig. 3. Log of the inverse of the spin-spin relaxation time ( $T_2^{-1}$ ), spin lattice relaxation time ( $T_1^{-1}$ ) and spin-spin relaxation time in the rotating frame ( $T_{1r}^{-1}$ ) as a function of inverse temperature for the LP sample. Activation energies obtained from the slopes are  $16.3 \pm 1.2$  kcal/mole,  $18.0 \pm 3.0$  kcal/mole and  $10.0 \pm 0.7$  kcal/mole respectively. The measuring frequency is 56.4 MHz.
- Fig. 4. The spin lattice relaxation time ( $T_1$ ) as a function of inverse temperature for the LP sample. The product  $T_1T$  is  $180 \pm 10$  K-sec.
- Fig. 5. Log of the inverse of the spin-spin relaxation time ( $T_2^{-1}$ ) and spin lattice relaxation time ( $T_1^{-1}$ ) as a function of inverse temperature for the HP sample. Arrows indicate the direction of the time temperature hysteresis.

- Fig. 6. Log of the inverse of the spin-spin relaxation time in the rotating frame ( $T_{1r}^{-1}$ ) and the lineshape as a function of time for the HP sample after the sample was heated to 460 K and was brought back to room temperature.
- Fig. 7. The eight pulse line shape and the peak locations of the  $\text{Th}_4\text{H}_{15}$  powder sample as a function of temperature using a  $\text{Ca}(\text{OH})_2$  single crystal as reference. The reference is oriented such that the major principal axis of the proton chemical shift tensor is parallel to the external magnetic field.
- Fig. 8. The relative shift of the proton resonance line in  $\text{Th}_4\text{H}_{15}$  powder sample as a function of temperature with respect to the same reference mentioned in Fig.7.

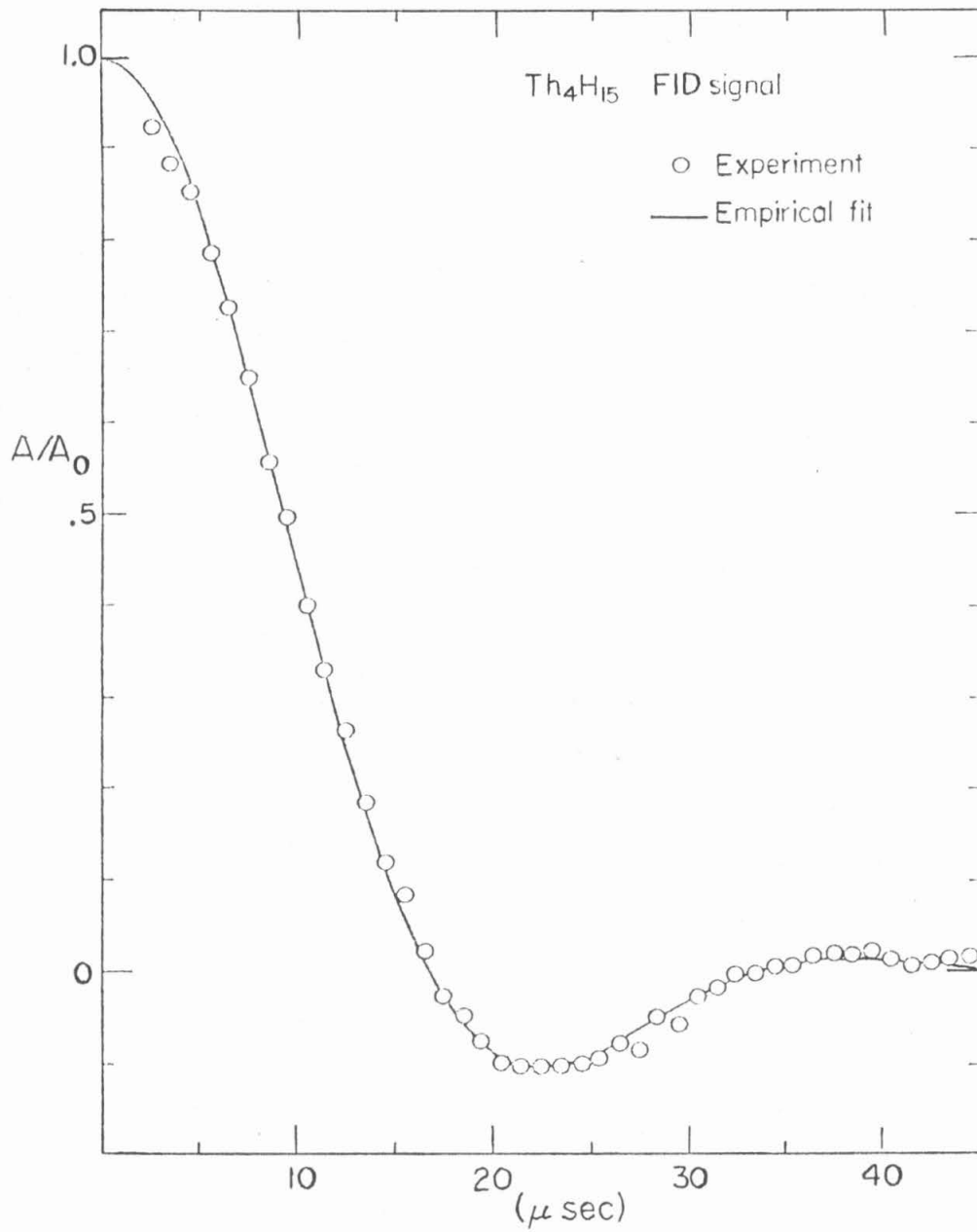


Fig. 1.

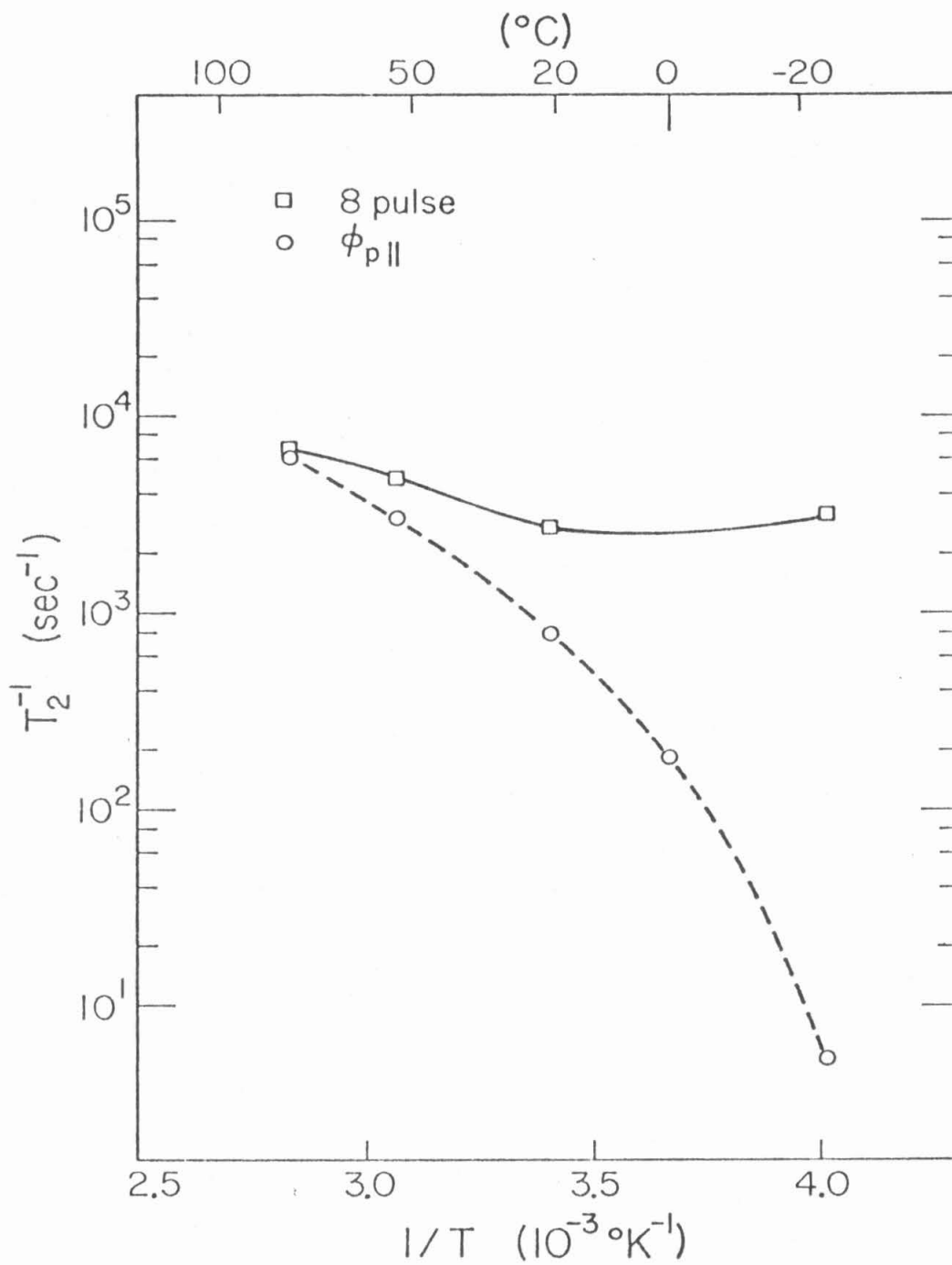


Fig. 2.

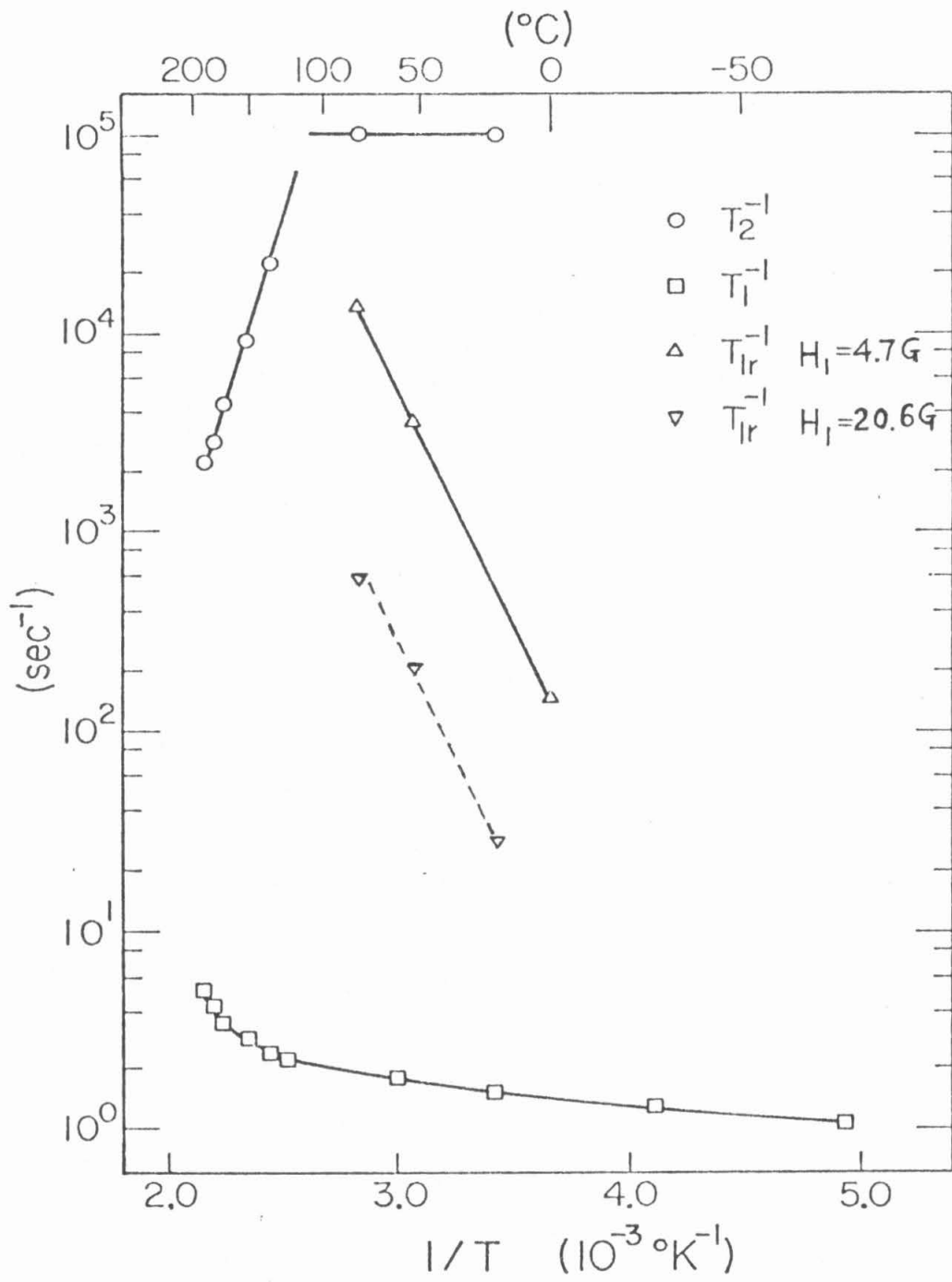


Fig. 3.

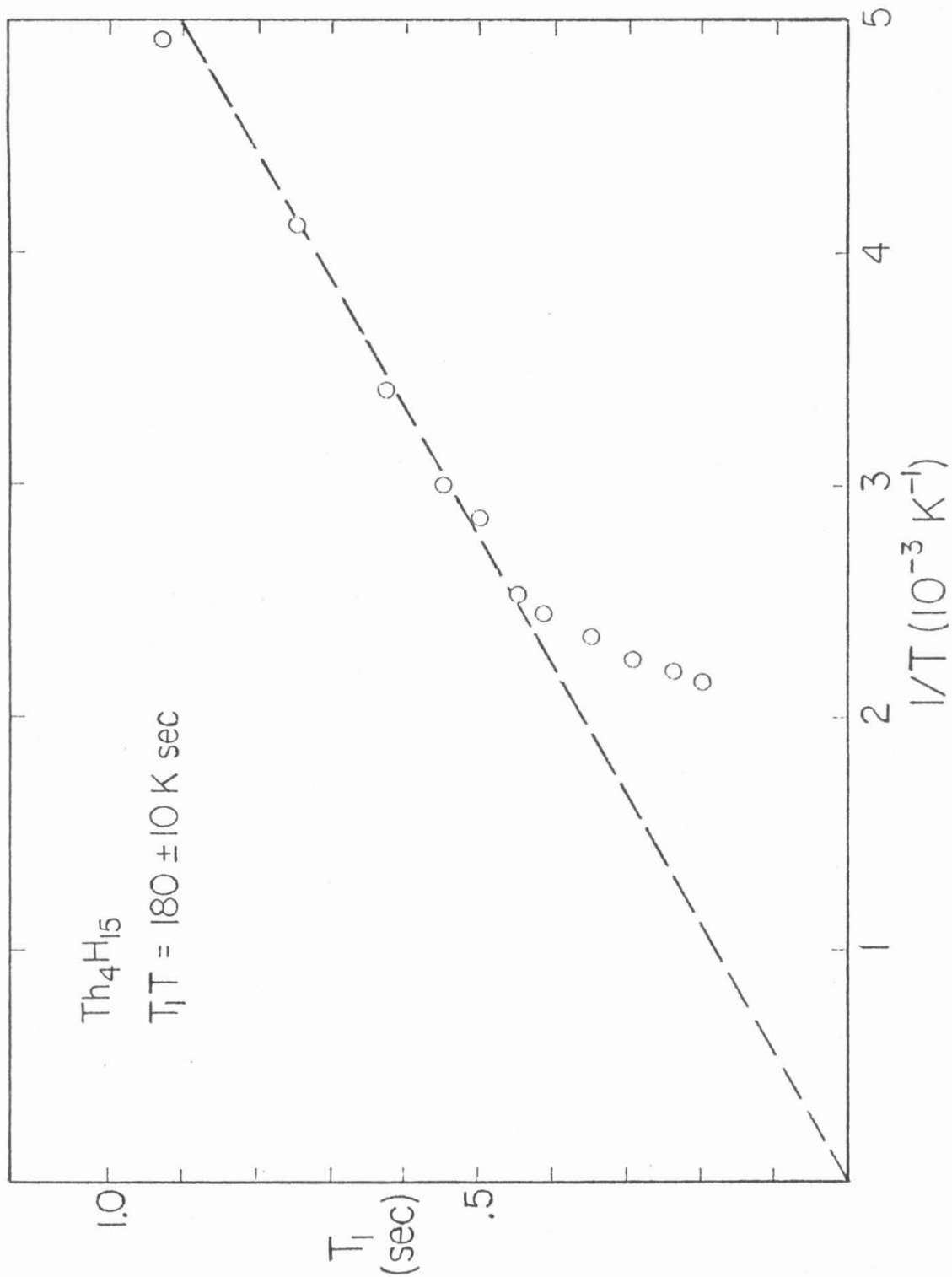


Fig. 4.

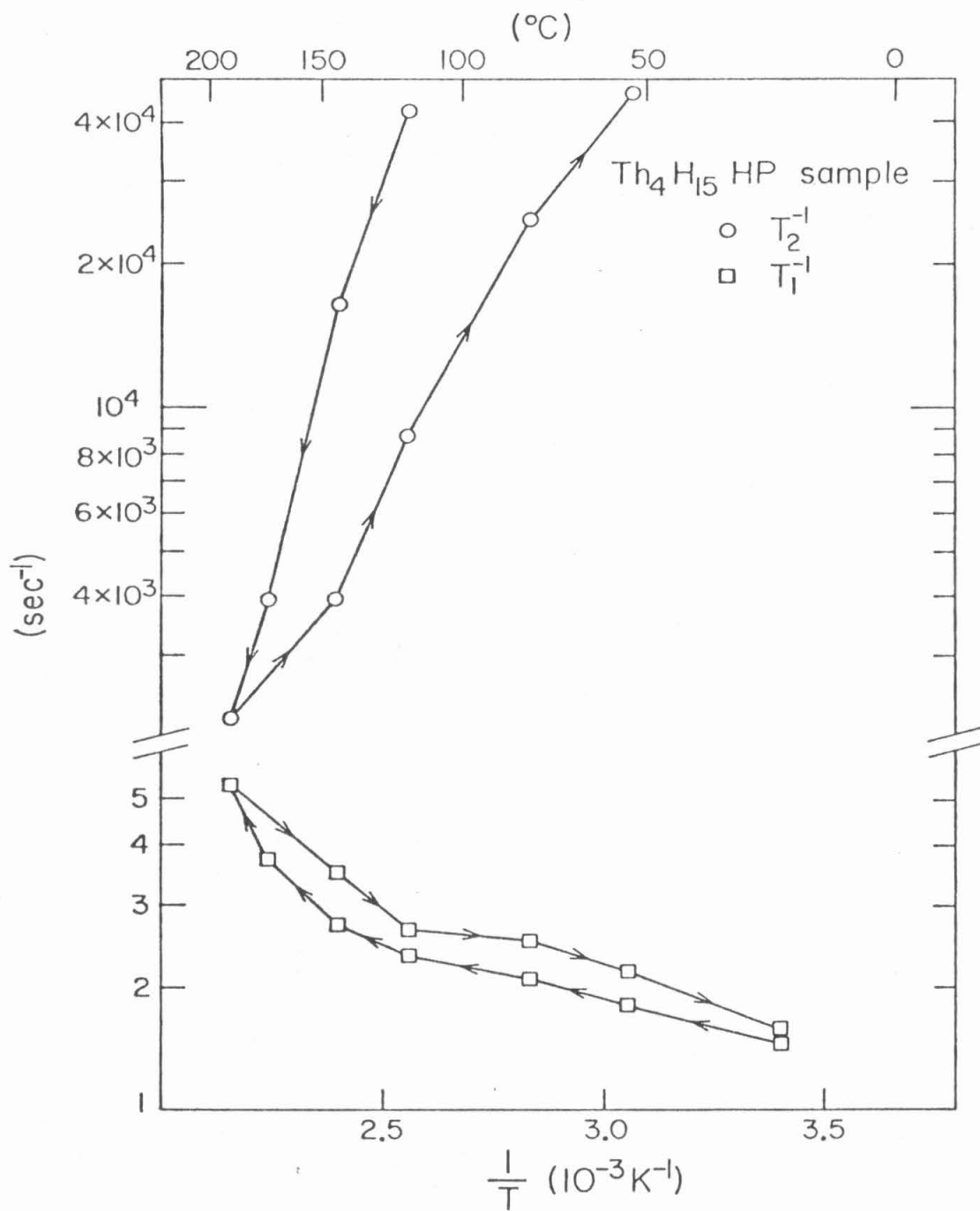


Fig. 5.

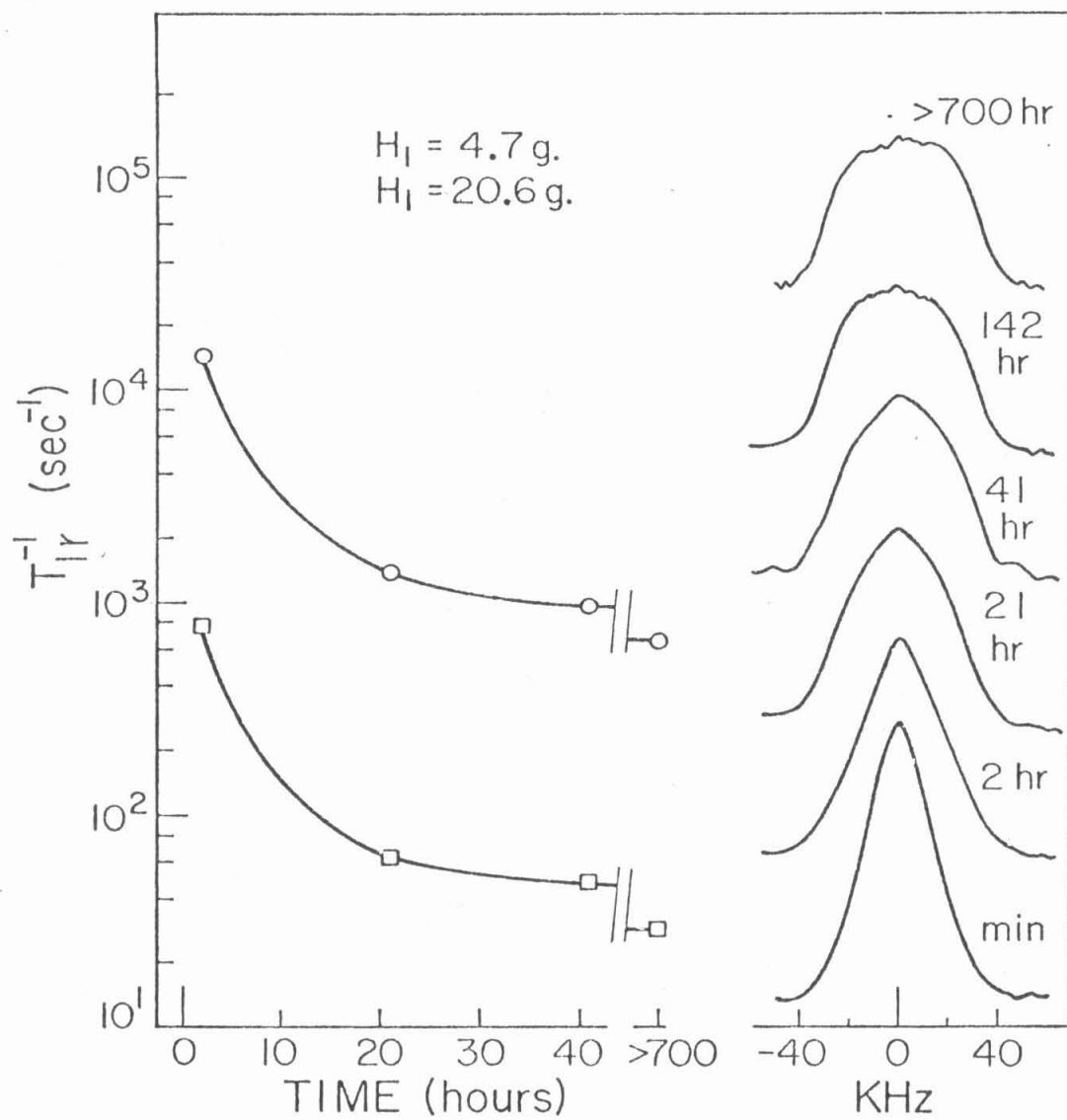


Fig. 6.

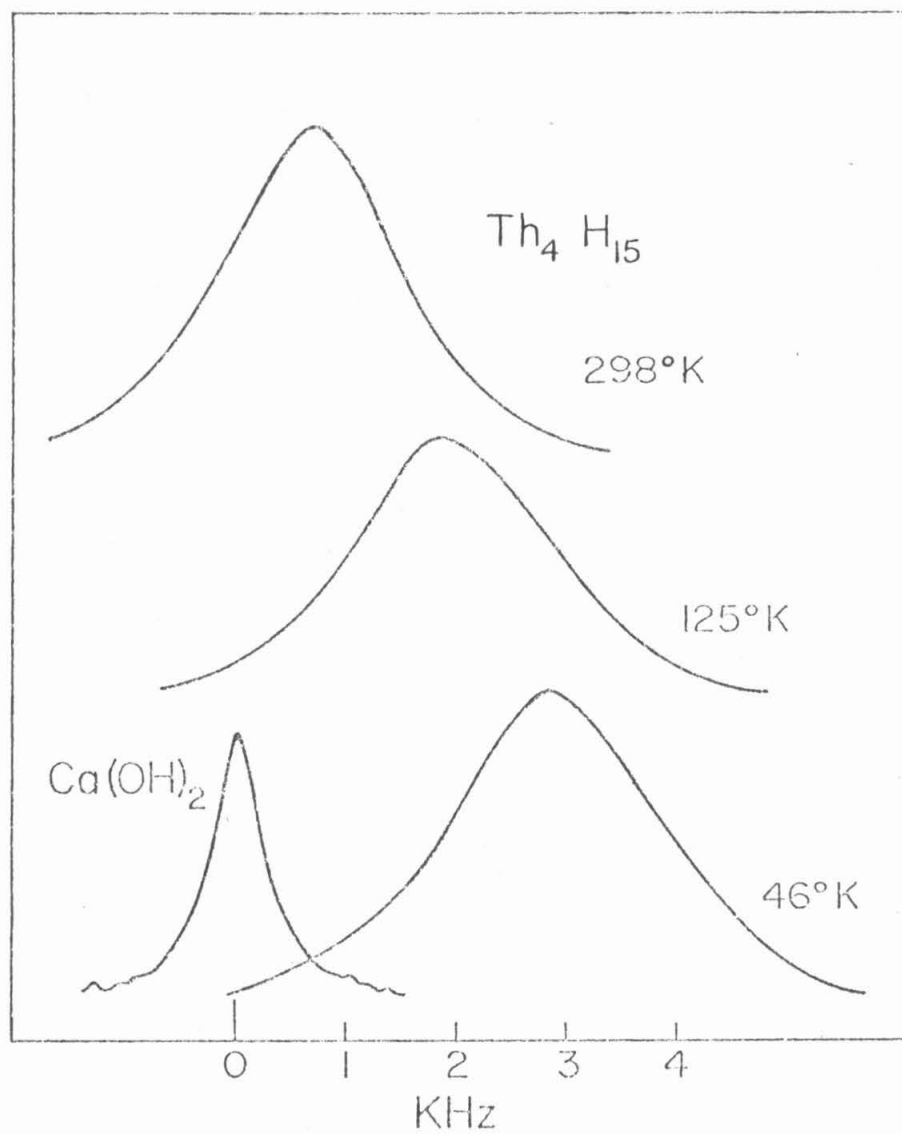


Fig. 7.

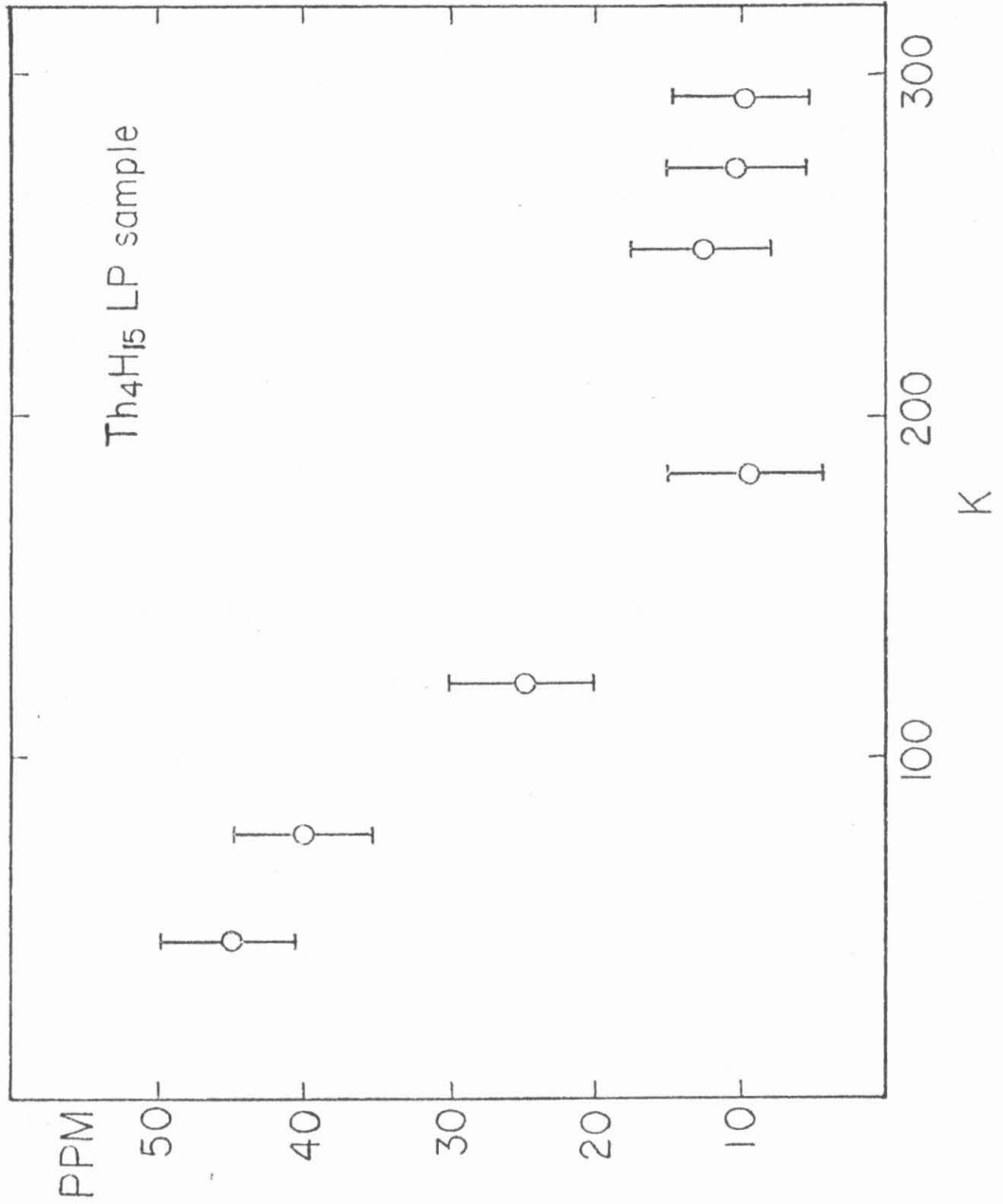


Fig. 8.